Assessment of Density Functionals for the High-Spin/Low-Spin Energy Difference in the Low-Spin Iron(II) Tris(2,2′-bipyridine) Complex**

Latévi Max Lawson Daku,*[a] Alfredo Vargas,[a] Andreas Hauser,[a] Antony Fouqueau,[b] and Mark Earl Casida[b]

In the iron(II) low-spin complex $[Fe(bpy)_3]^{2+}$, the zero-point energy difference between the ${}^5T_{2g}(t_{2g}^4e_g^2)$ high-spin and the ${}^1A_{1g}(t_{2g}^6)$ low-spin states, ΔE_{HL}^0, is estimated to lie in the range of 2500–5000 cm^{-1}. This estimate is based on the low-temperature dynamics of the high-spin→low-spin relaxation following the light-induced population of the high-spin state and on the assumption that the bond-length difference between the two states Δr_{HL} is equal to the average value of $\approx$0.2 Å, as found experimentally for the spin-crossover system. Calculations based on density functional theory (DFT) validate the structural assumption insofar as the low-spin-state optimised geometries are found to be in very good agreement with the experimental X-ray structure of the complex and the predicted high-spin geometries are all very close to one another for a whole series of common GGA (PB86, PW91, PBE, RPBE) and hybrid (B3LYP, B3LYP, PBE1PBE) functionals. This confirmation of the structural assumption underlying the estimation of ΔE_{HL}^0 from experimental relaxation rate constants permits us to use this value to assess the ability of the density functionals for the calculation of the energy difference between the HS and LS states. Since the different functionals give values from −1000 to 12000 cm^{-1}, the comparison of the calculated values with the experimental estimate thus provides a stringent criterion for the performance of a given functional. Based on this comparison the RPBE and B3LYP* functionals give the best agreement with experiment.*

1. Introduction

The electronic ground state of octahedral d^6 iron(II) complexes is either the high-spin (HS) ${}^5T_{2g}(t_{2g}^4e_g^2)$ state at low ligand-field strength or the low-spin (LS) ${}^1A_{1g}(t_{2g}^6e_g^0)$ state at high ligand-field strength. Complexes with an LS ground state for which the HS state is sufficiently close in energy can exhibit the phenomenon of spin-crossover, that is, the entropy-driven thermal transition from the LS state, populated at low temperatures, to the HS state, populated at higher temperatures.[1–3] For spin-crossover compounds, the zero-point energy difference between the two states $\Delta E_{HL}^o = E_{HS}^o - E_{LS}^o$ is typically of the order of 100–1000 cm^{-1}. For iron(II) systems the associated entropy difference is typically between 4 and 7 cm^{-1}K^{-1}.[4] X-ray structures of iron(II) spin-crossover compounds in the LS and HS states show that the spin transition is accompanied by a considerable elongation of the iron–ligand bond lengths. This is consistent with the promotion of two electrons from the essentially non-bonding t_{2g} orbitals to the antibonding e_g orbitals. Thus, for iron(II) spin-crossover complexes with an N_6 first coordination sphere, representing the vast majority of iron(II) spin-crossover complexes known to date, the change in Fe–N distance, $\Delta r_{HL} = r_{HS} - r_{LS}$, is found to be in the range of 0.16–0.22 Å.[5–11] The important lengthening of the iron–ligand bond and concomitant geometry changes give rise to a large increase of the molecular volume, $\Delta V_{HL} = V_{HS} - V_{LS}$. Experimentally, this has been evidenced by a change of the crystal volume associated with the spin transition of 15–30 Å^3 per molecular unit.[8,12–14] Such a large difference of the molecular volume makes the spin-crossover phenomenon sensitive to external pressure as well as to variations in the second coordination sphere,[15] and it is responsible for the cooperative effects often observed in neat spin-crossover compounds.

The spin transition can also be optically triggered by using laser excitation into metal–ligand charge transfer (MLCT) or d–d absorption bands to convert molecules efficiently from the LS state to the HS state. This discovery, made by McGarvey and Lawthers[16,17] and used to study the HS→LS relaxation in solution, was followed by the observation of Decurtins et al.[18,19] that at cryogenic temperatures, the HS→LS relaxation becomes so slow that iron(II) spin-crossover systems can be trapped quantitatively in the HS state, a phenomenon now known under the acronym of LIESST (light-induced excited spin-state trapping). The mechanism for the light-induced LS→HS conversion is schematically shown in Figure 1.

[a] *Dr. L. M. Lawson Daku, A. Vargas, Prof. A. Hauser*
Département de Chimie physique, Université de Genève
30 quai Ernest-Ansermet, 1211 Genève 4 (Switzterland)
Fax: (+41) 22-379-6103
E-mail: max.Lawson@chiphy.unige.ch

[b] *A. Fouqueau, Prof. M. E. Casida*
Institut de Chimie Moléculaire de Grenoble
Laboratoire d'Etudes Dynamiques et Structurales de la Sélectivité
Université Joseph Fourier (Grenoble I), 38041 Grenoble, (France)

[**] *Comparison of Density Functionals for Energy and Structural Differences between the High- $[{}^5T_{2g}(t_{2g}^4e_g^2)]$ and Low- $[{}^1A_{1g}(t_{2g}^6e_g^0)]$ Spin States of Iron(II) Coordination Compounds.*

Supporting Information for this article is available on the WWW under http://www.chemphyschem.org or from the author.

 DOI: 10.1002/cphc.200400584

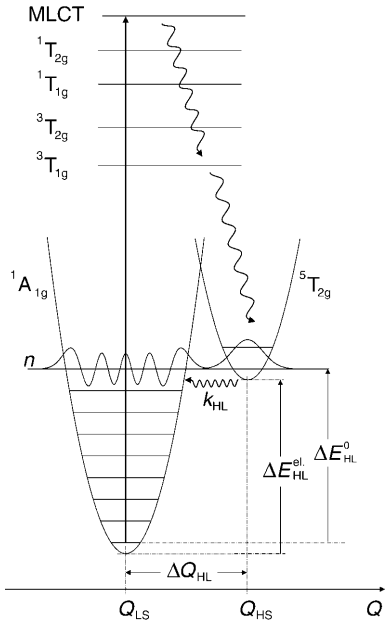

Figure 1. Configurational coordinate diagram along the totally symmetric breathing mode for an iron(II) complex with an LS $^1A_{1g}(t_{2g}^6)$ ground state. Only the potential wells of the ground state and the first excited state, namely the $^5T_{2g}(t_{2g}^4e_g^2)$ HS state are explicitly shown, higher excited ligand-field and metal–ligand charge transfer (MLCT) states are indicated schematically. The potential wells of the LS and HS states are plotted assuming equal vibrational frequencies, $\hbar\omega$, for the two states. Quantum efficiencies for the light-induced population of the HS state are generally close to unity.[26]

In a larger context LIESST is not restricted to spin-crossover compounds. It is likewise possible to achieve a light-induced population of the HS state in LS complexes such as the title complex $[Fe(bpy)_3]^{2+}$. Albeit, for these complexes the HS→LS relaxation is generally considerably faster than for spin-crossover complexes. As described in more detail below, the HS→LS relaxation is a non-adiabatic process[20] with pure tunnelling below $\approx$50 K and a thermally activated behaviour at elevated temperatures,[21,22] the most relevant parameters being Δr_{HL} and ΔE^o_{HL}. Whereas for spin-crossover complexes these are directly accessible experimentally (the former from X-ray crystallography, the latter in the form of ΔH^o_{HL} from the thermal transition curve extrapolated to $T\rightarrow 0$[23,24]), this is not the case for LS complexes.

Although a description of the electronic structure of the complexes based on ligand-field theory (LFT) serves to rationalise qualitatively most of the observations on spin-crossover systems to date,[25,26] LFT does not provide numerical values of the geometric and energetic factors at the required level of accuracy. We aim to improve our understanding of the photophysical properties not only of iron(II) spin-crossover systems but for iron(II) complexes in general using quantum chemical methods. Such methods are expected to give a description of the complexes that complements and quantitatively goes beyond their characterisation based on LFT alone. They are indeed essential for LS complexes for which the direct experimental determination of the relevant parameters is not possible.

Generally the large number of atoms in the complexes of interest, including $[Fe(bpy)_3]^{2+}$, precludes the use of computationally demanding high-level ab initio (i.e., wavefunction-based) methods, in contrast to methods based on density functional theory (DFT), which can efficiently be applied to systems of such size. In two previous papers,[27,28] we compared the results of density functional calculations with the results of high-level ab initio calculations for the description of the simple $[Fe(H_2O)_6]^{2+}$ and $[Fe(NH_3)_6]^{2+}$ complexes in the LS and HS states. In this paper, we extend our investigation of iron(II) complexes to the analysis of the low-temperature tunnelling process in the HS→LS relaxation dynamics for a LS complex. Specifically, we examine the extension of the relaxation model used for spin-crossover systems with the well-established correlation between the low-temperature tunnelling rate constant and the thermal transition temperature as a measure for ΔE^o_{HL} [26] to the LS complex $[Fe(bpy)_3]^{2+}$, and we relate the results to the relevant parameters as derived by density functional calculations.

2. The HS→LS Relaxation and the Zero-Point Energy Difference

HS→LS intersystem crossing may be observed for any iron(II) complex with a LS electronic ground state, that is, for iron(II) spin-crossover compounds but also for iron(II) LS compounds. However, because of the larger zero-point energy difference, the relaxation rates reported for the latter are considerably faster than for spin-crossover compounds. Thus, whereas for spin-crossover compounds at cryogenic temperatures, relaxation rate constants, $k_{HL}(T\rightarrow 0)$, are typically between 10^{-6} to 10^{-1} s^{-1}, those for LS complexes are on the microsecond-to-submicrosecond timescale. For $[Fe(bpy)_3]^{2+}$ (Figure 2), for instance, they vary between $\approx 10^4$ s^{-1} and $\approx 10^8$ s^{-1}, depending on the complex environment.[29–31]

As proposed by Buhks et al.,[20] the HS→LS relaxation in spin-crossover compounds of first-row transition metal ions is

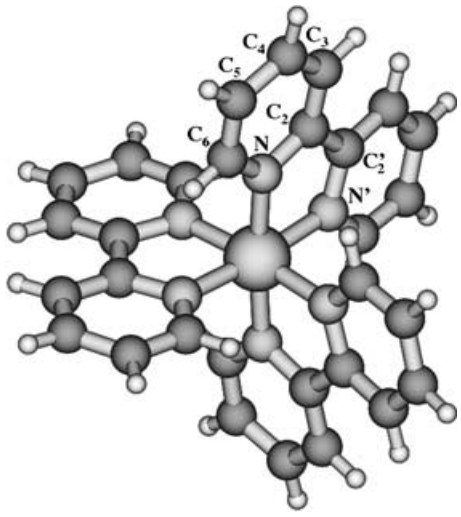

Figure 2. View of the X-ray structure[84] of $[Fe(bpy)_3]^{2+}$ in the LS state: the complex possesses a D_3 site symmetry. The atom labelling is indicated.

basically a radiationless non-adiabatic multiphonon process occurring between two distinct zero-order spin states characterised by different nuclear configurations. Given that the metal–ligand bond is shown to undergo the largest structural changes, the reaction coordinate Q is naturally taken as the totally symmetric breathing mode. Figure 1 shows a cross section of the LS and HS potential-energy surfaces along the Q coordinate. Harmonic potentials with equal force constants, f, and equal vibrational frequencies, $\hbar\omega$, are assumed for mathematical simplicity. Also, in this single-configurational-coordinate model, ΔQ_{HL}, the horizontal displacement of the two potential wells relative to each other is given by $\Delta Q_{HL}=\sqrt{6}\Delta r_{HL}$. The theory of nonadiabatic multiphonon relaxation leads to the following Equation (1) for the low-temperature tunnelling rate constant:[32]

$$k_{HL}(T\rightarrow 0)=\frac{2\pi}{\hbar^2\omega}\beta_{HL}^2|\langle\chi_n|\chi_0\rangle|^2 \quad (1)$$

For iron(II) systems with $\Delta S=2$ (S being the total electronic spin), the electronic-coupling matrix element $\beta_{HL}=\langle\Phi_{LS}|\mathscr{H}_{SO}|\Phi_{HS}\rangle$ comes from second-order spin–orbit coupling and takes on a value of $\approx$150 cm^{-1}.[20] The reduced energy gap $n=\Delta E^{o}_{HL}/\hbar\omega$ is a dimensionless measure for the vertical displacement of the potential wells of the initial HS and final LS states relative to each other. $|\langle\chi_n|\chi_0\rangle|^2$ is the Franck–Condon factor, that is, the squared overlap of the wavefunction of the lowest vibrational level of the HS state, from which the low-temperature relaxation exclusively occurs, with the wavefunction of the nth vibrational level of the LS state, as required by the principle of energy conservation. Inspection of Figure 1 shows the Franck–Condon factor to be a function of both ΔE^{o}_{HL} as well as ΔQ_{HL}. In the case of the harmonic approximation with equal force constants it can be expressed as Equation (2):

$$|\langle\chi_n|\chi_0\rangle|^2=\frac{S^n e^{-S}}{n!} \quad (2)$$

where [Eq. (3)]

$$S=\frac{(1/2)f\Delta Q_{HL}^2}{\hbar\omega} \quad (3)$$

The quantity S, the Huang–Rhys factor, is a dimensionless measure of the horizontal displacement of the potential wells relative to each other. Using the model values of $\hbar\omega=$ 250 cm^{-1} for the average vibrational frequency of the active modes, $f=2\times10^5$ dyn cm^{-1} for the corresponding force constant, and $\Delta Q_{HL}=\sqrt{6}\Delta r_{HL}=0.5$ Å for the bond-length difference expressed in terms of the totally symmetric stretch vibration, a value of S of 40–50 can be estimated.[32]

Figure 3 shows the low-temperature tunnelling rate constant on a logarithmic scale versus ΔE^{o}_{HL} calculated according to Equations (1)–(3), and using the above model values for the relevant parameters. Figure 3 includes the experimental points for a range of spin-crossover complexes from ref. [26]. (Note that whereas in ref. [26] the x axis corresponds to the transition temperature $T_{1/2}$ for the thermal spin transition, the x axis in Figure 3 corresponds to ΔE^{o}_{HL}. The two are intimately related:[22] $\Delta E^{o}_{HL}\approx\Delta H^{o}_{HL}\approx T_{1/2}\Delta S^{o}_{HL}$, with an average value of $\Delta S^{o}_{HL}\approx5$ cm^{-1}K^{-1}). The experimental points all lie within the range predicted for $S=40$–50. Figure 3 also indicates the above-mentioned range of low-temperature relaxation rate constants observed for $[Fe(bpy)_3]^{2+}$ doped into a series of inert crystalline host lattices. Assuming that for this complex, having the same $[FeN_6]$ coordination sphere as the spin-crossover compounds, the difference in bond length between the HS and the LS states is also $\approx$0.2 Å, a value for ΔE^{o}_{HL} of between 2500 and 5000 cm^{-1} may thus be estimated.

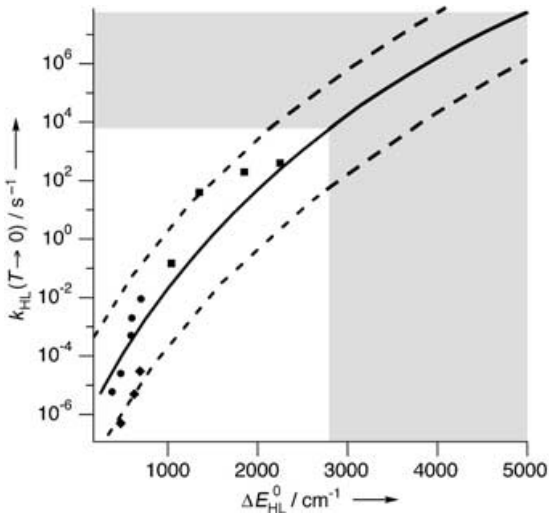

Figure 3. The low-temperature tunnelling rate constant, $k_{HL}(T\rightarrow0)$, on a logarithmic scale as a function of ΔE^{o}_{HL}. Theoretical curves were calculated using the model values as described in the text with an average value of $S=45$ (——) and the limiting values 40 and 50 (-----). The lozenges, circles and squares represent experimental values for a series of spin-crossover compounds with a $[FeN_6]$ first coordination sphere according to ref. [26]. The range of experimental values for the LS complex $[Fe(bpy)_3]^{2+}$ doped into different crystalline host lattices[15] is also indicated (shaded area).

The HS→LS relaxation can be accelerated by external pressure. This is due to the work-term-like expression $p\Delta V_{HL}$ giving an additional contribution to ΔE^{o}_{HL}. External pressure is most effective in the low-temperature tunnelling region. For spin-crossover compounds the tunnelling rate constant is typically enhanced by one order of magnitude per kbar, for low-spin systems the enhancement is somewhat smaller. For the title complex $[Fe(bpy)_3]^{2+}$, an acceleration of a factor of two at 10 K has been reported.[31] At comparatively low pressure, the low-temperature tunnelling rate constant as a function of pressure can be expressed as Equation (4):

$$k_{HL}(T\rightarrow0,p)=k_{HL}(T\rightarrow0,p=0)e^{\beta(T\rightarrow0)p} \quad (4)$$

where $k_{HL}(T\rightarrow0,p=0)$ is given by Equation (1) while the acceleration factor at low temperature $\beta(T\rightarrow0)$ is given by Equation (5):[33]

$$\beta(T\rightarrow0)\approx\frac{\Delta V_{HL}}{\hbar\omega}\ln\left(\frac{S}{n}\right) \quad (5)$$

For spin-crossover compounds with $n \approx 1$ and a model value for the difference in molecular volume $\Delta V_{HL} \approx 25$ Å^3, $\beta(T \rightarrow 0)$ takes on a value of 2 kbar^{-1} in line with the observation of a one order of magnitude acceleration per kbar external pressure. According to the above estimate of ΔE^{o}_{HL}, the reduced energy gap for $[Fe(bpy)_3]^{2+}$ is on the average around 15. With the experimental acceleration factor of $\beta = 0.69$ kbar^{-1}, and assuming the same model values for S and $\hbar\omega$ as above, ΔV_{HL} for $[Fe(bpy)_3]^{2+}$ is estimated to be of the same order as for the spin-crossover systems.

3. Theoretical Framework

The fact that the structure of $[Fe(bpy)_3]^{2+}$ cannot be experimentally characterised in the HS state makes the theoretical validation of the working hypothesis, $\Delta r_{HL} \approx 0.2$ Å, of utmost importance. We aim to validate this assumption by using a variety of density functional methods to achieve an accurate description of the geometry of the complex in the LS and HS states, and also at probing the ability of these methods to provide reliable estimates of the energy difference.

3.1. Outline of the Density Functional Formalism

Modern density functional calculations are based on the Kohn–Sham (KS) formulation of spin-density functional theory[34–39] wherein the ground-state energy E_0 of an N-electron system in an external local potential $v(\mathbf{r})$ is expressed as a functional of the spin-up $\rho_\uparrow(\mathbf{r})$ and spin-down $\rho_\downarrow(\mathbf{r})$ densities as follows in Equation (6):

$$E_0 = E_v[\rho_\uparrow,\rho_\downarrow] = T_s[\rho_\uparrow,\rho_\downarrow] + \frac{1}{2}\int\int d\mathbf{r}d\mathbf{r}' \frac{\rho(\mathbf{r})\rho(\mathbf{r}')}{|\mathbf{r}-\mathbf{r}'|} + \int d\mathbf{r}\rho(\mathbf{r})v(\mathbf{r}) + E_{XC}[\rho_\uparrow\rho_\downarrow] \quad (6)$$

where [Eq. (6a)]:

$$\frac{1}{2}\int\int d\mathbf{r}d\mathbf{r}' \frac{\rho(\mathbf{r})\rho(\mathbf{r}')}{|\mathbf{r}-\mathbf{r}'|} = J[\rho] \quad (6a)$$

$T_s[\rho_\uparrow,\rho_\downarrow]$ is the kinetic energy of the KS noninteracting N-electron system with the same spin-densities as the interacting system. $\rho(\mathbf{r}) = \rho_\uparrow(\mathbf{r}) + \rho_\downarrow(\mathbf{r})$ is the charge density and $J[\rho]$ is the Hartree self-interaction potential energy. The quantity $E_{XC}[\rho_\uparrow,\rho_\downarrow]$ thus defined by Equation (6) is the exchange–correlation (XC) energy. For dealing with this quantity whose analytical form is unknown, one distinguishes between the exchange and correlation contributions, noted $E_X[\rho_\uparrow,\rho_\downarrow]$ and $E_C[\rho_\uparrow,\rho_\downarrow]$, respectively. The exchange energy in Equation (7) reads:

$$E^{KS}_X[\rho_\uparrow,\rho_\downarrow] = -\frac{1}{2}\sum_{\sigma=\uparrow,\downarrow}\int\int d\mathbf{r}d\mathbf{r}' \frac{|\sum_{i\sigma} f_{i\sigma}\psi_{i\sigma}(\mathbf{r})\psi_{i\sigma}{}^*(\mathbf{r}')|^2}{|\mathbf{r}-\mathbf{r}'|} \quad (7)$$

where $f_{i\sigma}$ and $\psi_{i\sigma}(\mathbf{r})$ denote the occupation number and the spin orbital of the ith σ-type ($\sigma = \uparrow,\downarrow$) single-particle level of the KS noninteracting system. It takes on the same form as the Hartree–Fock (HF) exchange energy, thus reflecting the fact that its definition follows naturally from that of the HF exchange and similarly accounts for the Pauli exclusion principle, which tends to keep electrons of like spin apart. $E^{KS}_X[\rho_\uparrow,\rho_\downarrow]$ is an implicit functional of the spin densities because the KS spin orbitals are also functionals of the spin densities but their explicit dependence on $\rho_\uparrow(\mathbf{r})$ and $\rho_\downarrow(\mathbf{r})$ is unknown. Several schemes provide approximate exchange and correlation energy functionals explicitly in terms of the spin densities. The oldest is the local density approximation (LDA),[35] where it is assumed on the basis of the universality of the XC energy functional that the exchange and correlation energies per particle of a system at a given point $\mathbf{r}$ are those of a homogeneous electron gas, (HEG), whose constant spin densities are the ones of this system at $\mathbf{r}$. The LDA is valid for slowly varying densities. For atomic, molecular and solid systems characterised by rapidly varying densities, the LDA underestimates the exchange energy by about 14% and overestimates the correlation energy by a factor of approximately 2.5; quite often the two errors cancel.[38] The LDA, however, tends to overestimate bond energies.

The generalised-gradient approximation (GGA) remedies this deficiency by adding correction terms $\Delta E_\kappa[\rho_\uparrow,\rho_\downarrow]$, ($\kappa = X,C$), which depend on the gradients of the spin densities and which allow a better description of exchange and correlation, especially in the boundary region at the outer edges of atoms and where molecular binding occurs. The GGA XC functionals thus follow Equation (8):

$$\begin{aligned} E^{GGA}_{XC}[\rho_\uparrow,\rho_\downarrow] &= E^{GGA}_X[\rho_\uparrow,\rho_\downarrow] + E^{GGA}_C[\rho_\uparrow,\rho_\downarrow] \\ &= E^{LDA}_X[\rho_\uparrow,\rho_\downarrow] + \Delta E_X[\rho_\uparrow,\rho_\downarrow] + E^{LDA}_C[\rho_\uparrow,\rho_\downarrow] + \Delta E_C[\rho_\uparrow,\rho_\downarrow] \\ &= E^{LDA}_{XC}[\rho_\uparrow,\rho_\downarrow] + \Delta E_X[\rho_\uparrow,\rho_\downarrow] + \Delta E_C[\rho_\uparrow,\rho_\downarrow] \end{aligned} \quad (8)$$

where [Eqs. (8a) and (8b)]

$$E^{GGA}_X[\rho_\uparrow,\rho_\downarrow] = E^{LDA}_X[\rho_\uparrow,\rho_\downarrow] + \Delta E_X[\rho_\uparrow,\rho_\downarrow] \quad (8a)$$

and

$$E^{GGA}_C[\rho_\uparrow,\rho_\downarrow] = E^{LDA}_C[\rho_\uparrow,\rho_\downarrow] + \Delta E_C[\rho_\uparrow,\rho_\downarrow] \quad (8a)$$

The GGA enhances exchange while turning off correlation. This reproduces the expected trend that exchange turns on and correlation turns off (with respect to exchange) with increasing spin-density gradients,[40–43] but also with increasing charge density, or increasing spin polarisation measured locally by $\zeta(\mathbf{r}) = [\rho_\uparrow(\mathbf{r}) - \rho_\downarrow(\mathbf{r})]/\rho(\mathbf{r})$. In contrast to the LDA, the GGA is not related to a physically well-defined system. GGA functionals therefore are not "uniquely" defined in the sense that they can be derived in different ways. Nevertheless, the exchange part of the GGA XC energy gives the general form given in Equation (9):

$$E^{GGA}_X[\rho_\uparrow,\rho_\downarrow] = 2^{1/3}C_X\sum_{\sigma=\uparrow,\downarrow}\int d\mathbf{r}\rho_\sigma^{4/3}(\mathbf{r})F_X[2^{1/3}s_\sigma(\mathbf{r})] \quad (9)$$

with $C_X = -3/4\,(3/\pi)^{1/3}$, where the enhancement factor F_X depends on the reduced gradients $s_\sigma(\mathbf{r}) = |\nabla\rho_\sigma(\mathbf{r})|/(2(3\pi^2)^{1/3}\rho_\sigma^{4/3}(\mathbf{r}))$, and must give $F_X(0) = 1$ in order to reproduce the HEG results. The expressions for the GGA correlation functionals are more complicated.[37–39] The GGA improves the LDA description of the equilibrium geometries (typically giving longer bond lengths) and energetics. Further improvements were achieved with hybrid-XC energy functionals which are characterised by the fact that they include a contribution of the exact-exchange energy [Eq. (7)].[44,45] The correct amount of exact exchange to include in hybrid functionals is still a subject of on-going study.[46–48] Nowadays GGA and hybrid functionals are routinely used in DFT applications. Because there is no systematic approach for improving their quality, their performance must be assessed by comparing results for a variety of properties with accurate experimental data or with results from high-quality ab initio calculations.

3.2. DFT Characterisation of LS and HS States of Iron(II) Complexes

Whereas LFT serves to explain qualitatively most of the physical properties of spin-crossover complexes, it cannot provide structural and energetic parameters at the required level of accuracy. Unfortunately, the large size of spin-crossover complexes prohibits the use of detailed ab initio calculations. In principle, DFT offers a feasible alternative, but to date none of the numerous DFT-based methods has been acknowledged to constitute a foolproof approach to the problem of the description of spin-crossover compounds in their LS and HS states. Whereas optimised LS and HS geometries satisfactorily compare with available experimental geometries, the DFT methods often fail to describe the electronic contribution $\Delta E_{HL}^{el.}$ to the zero-point energy difference correctly. Thus, Paulsen et al.[49] noticed that commonly used GGAs—namely, the BLYP functional which combines Becke's 1988 (B or B88) exchange GGA[50] and the Lee–Yang–Parr (LYP) correlation GGA,[51] as well as the PW91 exchange–correlation GGA of Perdew and Wang[52–55]—give the expected LS ground state for the investigated iron(II) spin-crossover complexes, but they tend to give too high $\Delta E_{HL}^{el.}$ values. Baranović,[56] using the BP86 GGA made from the B exchange and Perdew's 1986 (P86) correlation[57] functionals, obtained similar results and proposed an empirical parameter to scale calculated $\Delta E_{HL}^{el.}$ values appropriately.

In contrast Paulsen et al.[49] also showed that the HS state is stabilised with respect to the LS state and is falsely predicted to be the ground state if the B3LYP functional is used. This functional is the workhorse of the hybrid-XC energy functionals. Omitting the explicit reference to the spin densities in the notation of the functionals, it reads [Eq. (10)][58]

$$E_{XC}^{B3LYP} = (1-a_0)E_X^{LDA} + a_0E_X^{KS} + a_X\Delta E_X^{B} + (1-a_C)E_C^{VWM} + a_CE_C^{LYP} \quad (10)$$

where E_C^{VWN} is the VWN parameterisation corresponding to the random phase approximation correlation energy.[59] ΔE_X^B stands for the nonlocal component (i.e., gradient corrections) of the Becke's 1988 exchange GGA; and the coefficients $(a_0,a_X,a_C) = (0.20,0.72,0.81)$ are the ones determined by Becke,[45] originally for the B3PW91 hybrid, by fitting to a data set of atomisation energies. Given the incorporation of an exact-exchange contribution in hybrid functionals, the B3LYP behaviour reported by Paulsen et al.[49] can be ascribed to the fact that such functionals inherit from the HF scheme the tendency towards over stabilising states of high spin multiplicity with respect to states of lower multiplicity.

The preference of the B3LYP for a high-multiplicity ground state in iron(II) complexes was also observed by Reiher, Salomon and Hess[60] who evidenced a linear dependence of $\Delta E_{HL}^{el.}$ on the amount a_0 of exact-exchange admixture in Equation (10). They recommended a reduced a_0 value of 0.15 for which the resulting B3LYP* functional correctly predicts the ground state of a number of iron(II) complexes.[60,61] Nevertheless, in the particular case of the spin-crossover Fe(1,10-phenantroline)$_2$(NCS)$_2$ complex, even the B3LYP* functional incorrectly gives the HS state as the ground state.[62] As pointed out by Reiher, this suggests that the amount of exact exchange may be further reduced in the case of this complex. As previously mentioned, the question of the amount of exact exchange to include in hybrid functionals is a subject of ongoing study,[46–48] and although an improvement is often observed when exact exchange is admixed in density functional approximations, so far no sound reasons have been established as to why hybrid functionals should perform better than modern GGAs, especially with regard to estimating energy gaps between states of different spin multiplicities.

This ambiguous situation regarding the reliability of DFT methods for the study of spin-crossover and related systems, combined with the lack of a calibration of density functionals against accurate ab initio results for simpler iron(II) complexes, led us to perform a comparison of density functionals for energy and structural differences between the HS and LS states of the HS $[Fe(H_2O)_6]^{2+}$ complex.[27] We used the BP86, BLYP, PW91 GGAs, the recent exchange–correlation GGA of Perdew–Burke–Ernzerhof (PBE)[63,64] and the revised PBE (RPBE) functional of Hammer, Hansen and Nørskov[65] as well as the B3LYP hybrid, and compared the DFT results with results obtained at the complete active space SCF (CASSCF), second-order-perturbation-theory-corrected CASSCF (CASPT2), and spectroscopy-oriented configuration interaction (SORCI[66]) levels. Whatever the theoretical method, the HS state was correctly reproduced as the ground state for this HS system, $(\Delta E_{HL}^{el.} < 0)$. A good agreement was achieved between the experimental geometries of the complex in its HS state and the ones obtained at the CASSCF and DFT levels. All theoretical methods consistently predicted quite similar geometries for the excited LS state. The situation was quite different with regard to the energetics. Comparison of the DFT molecular energy gaps with the best ab initio estimate revealed that the functionals, with the noticeable exception of the B3LYP and RPBE, systematically underestimate the stability of the HS state with respect to the LS state by giving too small $|\Delta E_{HL}^{el.}|$ values. The B3LYP and RPBE functionals on the other hand were shown to be the most reliable of the functionals. Subsequently,

the comparison was extended to the HS $[Fe(NH_3)_6]^{2+}$ complex and additional functionals[28] (Paper II of the series), and the overall best agreement for the energetics of the two complexes was obtained for the PBE1PBE hybrid functional (also known as PBE0). This functional is of the parameter-free form as shown in Equation (11):

$$E_{XC}^{hybrid} = E_{XC}^{GGA} + a_0(E_X^{KS} - E_X^{GGA}) \quad (11)$$

with $a_0 = 1/4$, proposed by Perdew, Ernzerhof and Burke[46,47] and for which the GGA contribution is given by the PBE functional.[67,68]

The present theoretical study of the LS $[Fe(bpy)_3]^{2+}$ complex, for which high-quality ab initio calculations clearly are not manageable, but for which experimental data are available, provides a further assessment of the performance of the density functionals. The following sections deal with the characterisation of the trigonal complex in the LS and HS states using the BP86, PW91, PBE, RPBE, B3LYP, and B3LYP* and PBE1PBE functionals.

Computational Section

The Amsterdam density functional (ADF)[69] program package was used to carry out calculations with the BP86, PW91, PBE and RPBE GGAs. To probe the influence of the choice of the basis, two qualities of Slater-type orbital (STO) basis sets from the ADF basis set database were employed for the Fe, N, C and H atoms, namely, the double-ζ "DZ" and triple-ζ polarised "TZP" STO basis. Computations involving the B3LYP, B3LYP* and PBE1PBE hybrids were performed with the Gaussian[70] program package, using for all atoms either the triple-ζ polarised Gaussian-type orbital (GTO) basis "TZVP" of Schäfer, Huber and Ahlrichs[71] or the 6-311+G** basis set,[72–75] which is a triple-ζ polarised GTO basis set with sets of diffuse functions on the Fe, N, and C atoms. For comparison purposes, the Gaussian package was also used to perform calculations with the PBE GGA, as well as calculations at the HF level. Fractional occupation numbers were used in the ADF calculations but are not allowed in the present implementation of Gaussian (except as an intermediate step in the SCF convergence strategy[76]). For the LS state spin-restricted and for the HS state spin-unrestricted calculations were performed constraining M_S, the projection of the total electronic spin along a reference axis, to $M_S = 0$ and $M_S = +2$, respectively. In all cases, the symmetry for the $[Fe(bpy)_3]^{2+}$ complex was constrained to D_3. Results were visualised using the MOLEKEL[77] and MOLDEN[78] software.

4. Results and Discussion

4.1. LS and HS States

In carrying out the DFT calculations, we typically seek the lowest-lying state of each spatial and spin symmetry.[36] According to LFT, the LS and HS states should be the $^1A_{1g}(t_{2g}^6)$ and $^5T_{2g}(t_{2g}^4e_g^2)$ states, respectively. These states do not appear directly as such in the DFT calculations because the $[Fe(bpy)_3]^{2+}$ complex is not of O_h symmetry but of D_3 symmetry. In particular, this means that the $^5T_{2g}(t_{2g}^4e_g^2)$ state actually splits into two states, one of ^5E symmetry and one of $^5A_1$ symmetry. In addition, there exists for complexes such as $[Fe(bpy)_3]^{2+}$ a high density of states sometimes making the identification of the lowest-lying state of each spatial and spin symmetry difficult. For these reasons, and to seek additional chemical insight, we performed a careful analysis of the resulting KS molecular orbitals (MOs) and orbital energy levels, thus verifying that the characterised electronic states indeed correspond to the ligand-field $^1A_{1g}(t_{2g}^6)$ and $^5T_{2g}(t_{2g}^4e_g^2)$ states of interest. MOs are indeed unavoidable tools for understanding molecular bonding and structure and for discussing chemical and physical phenomena. Moreover, although this is not the case for virtual MOs, occupied orbitals can be "observed" by electron-momentum spectroscopy,[79,80] scanning tunnelling microscopy[81] and very recently by tomographic imaging based on femtosecond laser technology.[82]

The different DFT calculations performed for a given M_S value result in similar KS orbital energy levels. Thus, for $M_S = 0$, there is a full occupation of the lowest-lying orbital energy levels from which one readily deduces that the converged KS determinants characterise the lowest-lying electronic state of $^1A_1$ symmetry. More insight into the electronic structure of $[Fe(bpy)_3]^{2+}$ in this state is reached through the inspection of the frontier KS orbital levels given in Figure 4 for the PBE/TZP calculation.

From a MO viewpoint, the existence of chemical bonding between the metal and the ligands is seen in the composition of the "metallic" KS MOs, which are no longer pure metal orbitals. These MOs with a Fe(3d) main parentage, which belongs to the frontier MOs, are the highest-occupied $25a_1$ and 44e levels and the virtual 47e level. Other virtual levels of e or a_1 symmetry can exhibit small but noticeable "metallic" contributions as a result of the complex orbital interactions of σ and π types occurring in $[Fe(bpy)_3]^{2+}$. The unoccupied "metallic" level results from σ-type orbital interactions and is antibonding. It contains a significant admixture of ligand contribution in contrast to the $25a_1$ and 44e levels, which are mainly nonbonding and remain "metallic" in nature. It can thus be concluded that the highest-occupied levels originate from the trigonal splitting of the octahedral $Fe(t_{2g})$ level whereas the virtual "metallic" level comes from the antibonding octahedral $Fe(e_g)$ level. Hence their occupation shows that the characterised singlet state relates to the ligand-field $^1A_{1g}(t_{2g}^6)$ state.

The characterisation of the complex in the HS state proved to be trickier than that of the LS state as the two possible HS states, namely the $^5A_1$ and ^5E states which result from the trigonal splitting of the octahedral $^5T_{2g}$ state, had to be accounted for. Within D_3 symmetry the two states were found to be nearly degenerate. The near-degeneracy of the $^5A_1$ and ^5E is due to the fact that passing from one state to the other corresponds mainly to a charge redistribution within the nonbonding KS orbital levels of $Fe(t_{2g})$ parentage, which hardly affects the metal–ligand bond (see below for a more detailed discussion). In the following, the two trigonal components of the HS state are discussed in more detail. Due to the difference in the way they handle degenerate states, Gaussian was restricted to the $^5A_1$ component, whereas ADF allowed the characterisation of both the $^5A_1$ as well as the ^5E trigonal components of the HS $^5T_{2g}$ state.

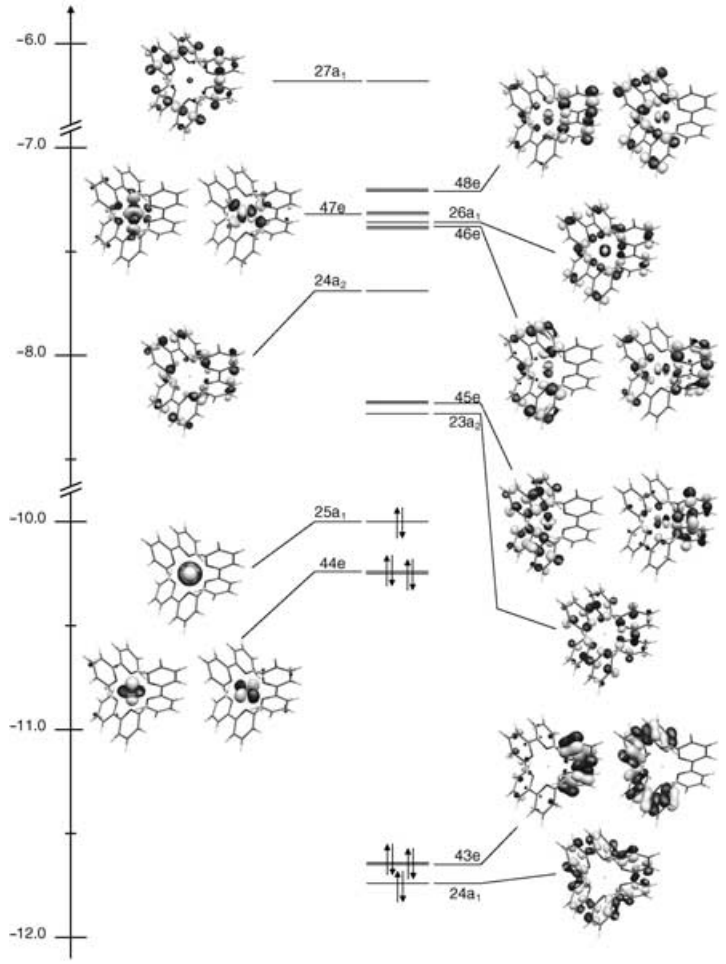

Figure 4. Frontier KS MOs of $[Fe(bpy)_3]^{2+}$ in the $^1A_1$ state (PBE/TZP results; eigenvalues in eV).

For the HS ^5E state, ADF gave similar electronic structures for all functionals and irrespective of the quality of the basis set. This is illustrated by the diagram of the frontier KS orbital levels of Figure 5, which has been constructed from the PBE/TZP results. For clarity, only the frontier MOs with significant metallic character are drawn and the spin-up and spin-down orbital levels are represented separately. The spin-down orbital levels of Figure 5 remain similar in their energy ordering and in the shapes of their orbitals to the ones reported for the LS case. In particular, the 44e and $25a_1$ spin-down-orbital levels are also nonbonding and of octahedral Fe(t_{2g}) parentage, while the 47e spin-down-orbital level results from antibonding σ-type metal–ligand interactions and is of octahedral Fe(e_g) parentage. The $24a_1$, 43e and 45e spin-up-orbital levels are the only spin-up frontier levels with a significant metallic character, the $24a_1$, 43e levels being of Fe(t_{2g}) parentage and the 45e level of Fe(e_g) parentage. They possess more ligand contributions than their spin-down counterparts do, and their energies and ordering also differ from those of their spin-down counterparts. When considering the occupation of the KS levels, it appears that the characterised electronic state is obtained from the LS state by a two-electron excitation with spin-flip within the subset of the metallic frontier-orbital levels of the LS state: using the notation of Figure 4, this d–d excitation corresponds to the promotion of two electrons from the $25a_1$ and 44e spin-down KS levels of octahedral Fe(t_{2g}) parentage into the 47e spin-up level of Fe(e_g) parentage. Finally, from the orbital degeneracy due to the occupation of the highest spin-down orbital level of e symmetry by a single electron (Figure 5), it can be concluded that the characterised electronic state is the $M_S=+2$ sublevel of the ^5E manifold that results from the trigonal splitting of the LFT $^5T_{2g}(t_{2g}^4e_g^2)$ state.

The characterisation of the HS $^5A_1$ component could be performed with both software packages. The electronic structure of the complex in this state is depicted in Figure 6 by the diagram of the frontier KS MOs constructed from the PBE/TZP results. The representation of the MOs is again limited to those with noticeable metallic character. A comparison between this diagram and the diagram obtained for the HS ^5E state (Figure 5) illustrates that, in essence, the two HS states differ by the nature of the highest-occupied spin-down KS level of octahedral Fe(t_{2g}) parentage: namely, the 44e level for the ^5E state and the $25a_1$ level for the $^5A_1$ state. When passing from the HS ^5E state to the HS $^5A_1$ state, the $25a_1$ spin-down level is slightly stabilised in energy whereas the 44e spin-down level is comparatively more destabilised. The opposite trend is observed for their spin-up counterparts which are labelled 43e and $24a_1$ for the ^5E state, and 43e and $25a_1$ for the $^5A_1$ state: the e level shows a moderate stabilisation and the a_1 level undergoes a very strong destabilisation. As for the antibonding e levels of Fe(e_g) parentage, namely the occupied 45e spin-up level and the virtual 47e spin-down level for the ^5E state, and the 48e spin-down level for the $^5A_1$ state, they become moderately destabilised. The comparison of the two diagrams thus shows that the frontier KS levels with a metallic character are the ones which suffer the largest changes, and more especially that the nonbonding spin-down and spin-up levels of Fe(t_{2g}) parentage are the most affected metallic frontier levels. That is, the difference in the electronic structure of $[Fe(bpy)_3]^{2+}$ in the two HS states is mainly located in the metal-centred nonbonding levels of octahedral Fe(t_{2g}) parentage.

4.2. Optimised Geometries

4.2.1. Geometries in the LS State

The X-ray crystal structure of the $[Fe(bpy)_3]^{2+}$ cation has been reported twice so far.[83,84] In the following we exclusively refer to the experimental data published by Dick, who solved the crystal structure of $[Fe(bpy)_3](PF_6)_2$ at 293 K.[84] The compound crystallises in the space group $P\bar{3}c1$ and the experimental metal–ligand bond lengths of 1.967 Å are typical for the complex in the LS ground state. It possesses D_3 site symmetry. For

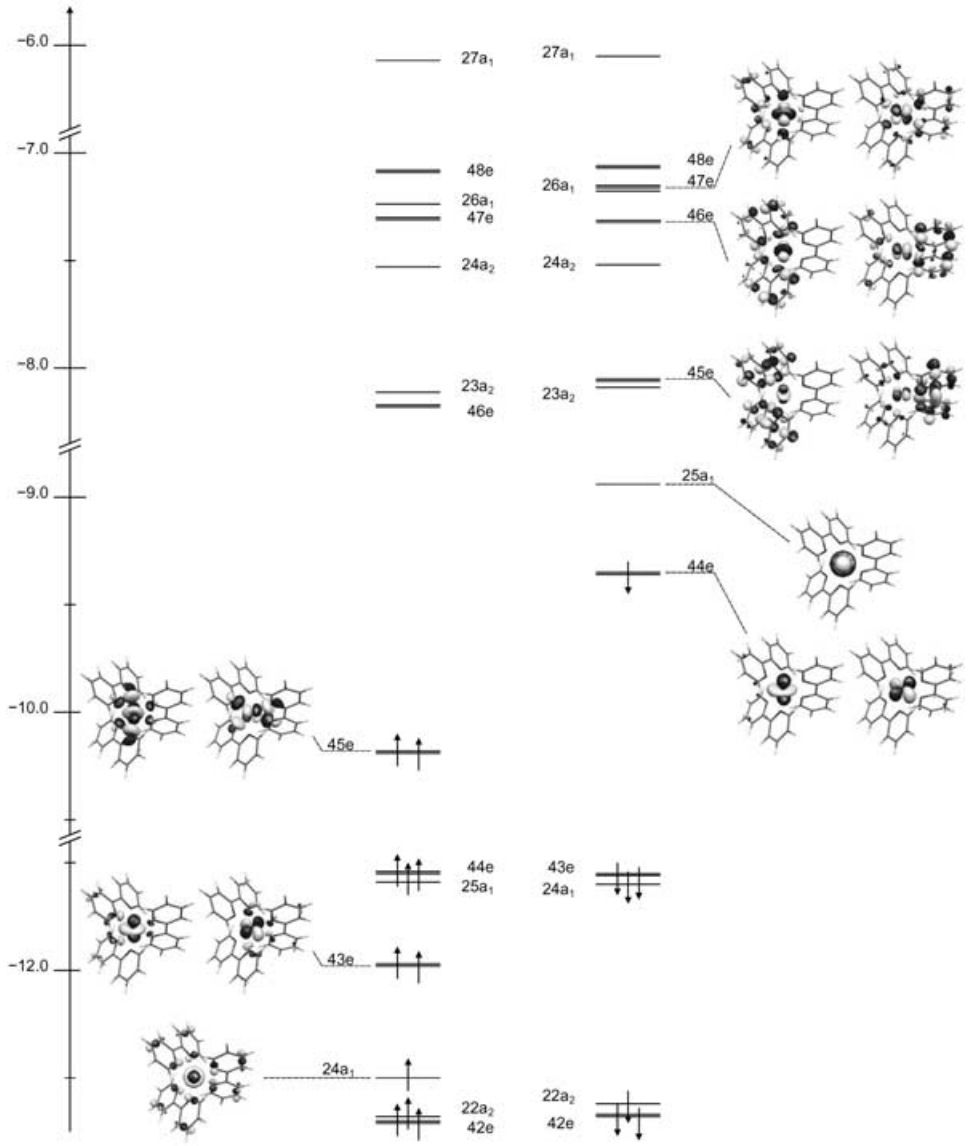

Figure 5. Frontier KS MOs of $[Fe(bpy)_3]^{2+}$ in the ^5E state: for clarity, only the MOs with noticeable metallic character are represented (PBE/TZP results; eigenvalues in eV).

this experimental structure, selected distances and values of the angles β, γ, τ and θ, which characterise the arrangement of the ligands around the Fe centre (see Figure 7), are summarised in Table 1.

The values obtained for the same structural parameters of the optimised ground-state geometries from DFT are also reported in Table 1. The calculated geometries are all similar to one another irrespective of the functional and the quality of the basis set, and compare well with the experimental structure. For instance, all calculations led to a $N–C_2$ bond which is longer than the $N–C_6$ bond in agreement with experiment. However, the optimised geometries prove to be more expanded than the experimental geometry since, with the exception of the $C_2–C_2'$ and Fe–N bonds, the bond lengths found for the calculated structures tend to be systematically larger than those found experimentally. Given that our study is performed in the gas phase and therefore does not account for the packing and counter-ion effects present in the solid state, there is no reason as to why the experimental and calculated geometries should strictly match.

A more detailed analysis shows that the tendency of the optimised bond lengths of the pyridinyl rings to be larger than experimentally observed is most pronounced for the double-ζ STO DZ basis set and less pronounced for the GTO 6-311+G** basis set. It is least pronounced for the triple-ζ polarised GTO TZVP and STO TZP basis sets, which give identical results when used with the PBE functional. This trend corresponds to a shrinking of the aromatic rings with the quality of the basis set. With the exception of the dihedral angle γ, the calculated values of the angular parameters are close to those found for the X-ray structure to within ≈ 1 degree, reflecting analogous arrangements of the ligands in the experimental and calculated structures. The γ values are larger for the GTO basis sets than for the STO basis sets. This basis-set dependence and the important differences of about 3–6 degrees between the experimental and calculated γ values can be explained by the fact that the deformations along this angular coordinate are associated with floppy modes. On the whole, the best agreement between the calculated and experimental geometries of the ligands is observed for the hybrid functionals, in line with the acknowledged good performance of the hybrids for the description of the molecular structures of covalently bound main group elements.[39]

The optimised metal–ligand bond lengths increase with the quality of the basis sets used. Thus the shortest Fe–N distances are obtained for the DZ basis set as this allows the lack of flexibility of this basis set for describing the Fe atom (especially with regard to the important electron correlation in d-space) to be compensated for by the use of basis functions centred on the neighbouring N atoms. Longer Fe–N distances result from the use of the larger basis sets, but the Fe–N distances obtained for the 6-311+G** basis set are still slightly shorter than those obtained for the TZVP and TZP basis sets, presuma-

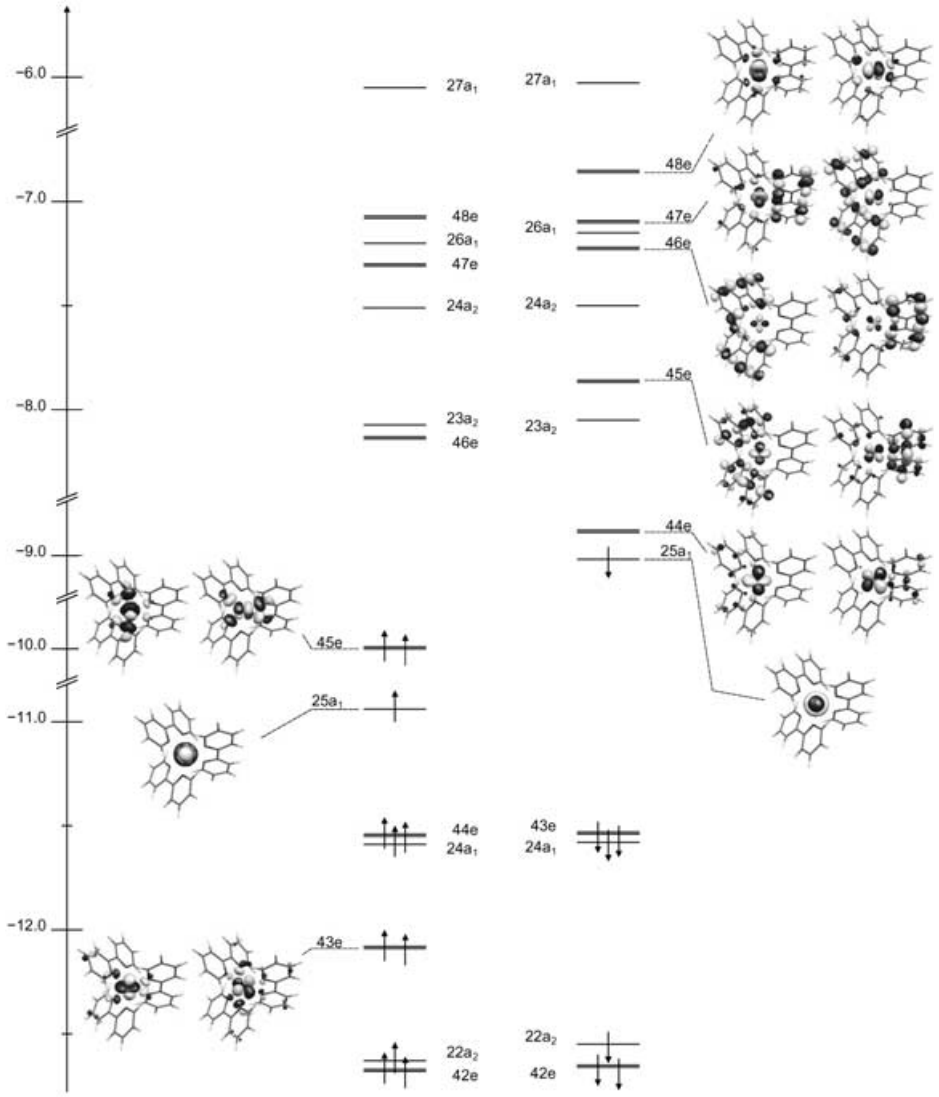

Figure 6. Frontier KS MOs of $[Fe(bpy)_3]^{2+}$ in the $^5A_1$ state: for clarity, only the MOs with noticeable metallic character are represented (PBE/TZP results; eigenvalues in eV).

bly for the same reason as for the DZ basis set. The comparable quality of the TZP and TZVP basis sets is also illustrated by the fact that they lead to equal Fe–N distances when used with the PBE functional. With regard to the different functionals used in this study, the values of the optimised Fe–N bond length are lower for the BP86, PW91 and PBE GGAs than for the RPBE GGA and the hybrid functionals. One also notes that the increase of the exact-exchange contribution from 15% in the B3LYP* functional to 20% in the B3LYP functional is accompanied by a lengthening of the Fe–N distance of 0.014 Å. Similarly, the admixture of 25% exact-exchange to the PBE functional as in the PBE1PBE hybrid gives rise to an increase of the Fe–N distance by 0.022 Å. We thus conclude that hybrid functionals tend to give longer metal–ligand bond lengths than the GGAs, and that the more important the exact-exchange contribution the longer the metal–ligand bond. Figure 8 illustrates this by showing the evolution of the Fe–N bond length in the LS state as a function of the amount a_0 of exact exchange in the B3LYP and

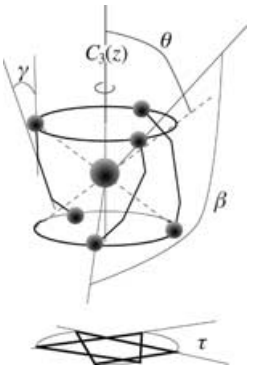

Figure 7. Angles characterising the spatial arrangement of the ligands around the metal centre in $[Fe(bpy)_3]^{2+}$. β is the bite angle (β = N–Fe–N′), γ the dihedral angle between the ligand moieties (γ = N–C_2–C_2′–N), τ the twist angle and θ the angle between the z axis and the generator of the cone on which the nitrogen atoms are located.

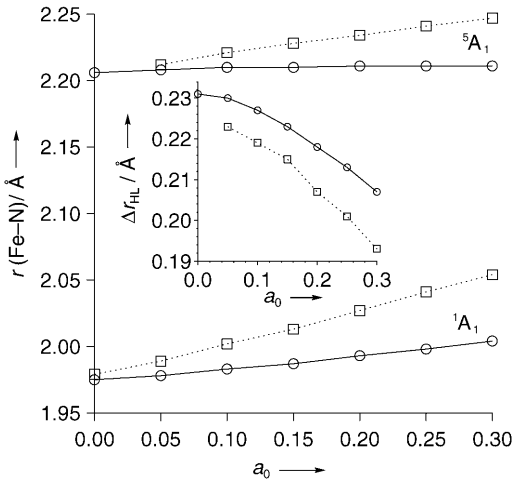

Figure 8. Evolution of the Fe–N bond length, in the LS and HS $^5A_1$ states, with the value of the a_0 coefficient of the exact-exchange contribution in the PBE1PBE (●) and B3LYP (■) hybrids; the inset gives the a_0 dependence of Δr_{HL}; (results of geometry optimisations performed using the TZVP basis set).

Table 1. Comparison between experimental and theoretical $^1A_1$ $[Fe(bpy)_3]^{2+}$ geometries.

	Exp.[84]	ADF							
		BP86		PW91		PBE		RPBE	
		DZ	TZP	DZ	TZP	DZ	TZP	DZ	TZP
				Bond lengths [Å]					
Fe–N	1.967	1.956	1.978	1.954	1.971	1.955	1.975	1.979	2.003
N–C_2	1.359	1.384	1.369	1.380	1.365	1.382	1.367	1.388	1.373
N–C_6	1.338	1.367	1.354	1.364	1.351	1.366	1.353	1.372	1.359
C_2–C_2'	1.471	1.462	1.463	1.459	1.461	1.460	1.462	1.469	1.471
C_2–C_3	1.377	1.402	1.400	1.400	1.397	1.401	1.399	1.408	1.406
C_3–C_4	1.374	1.399	1.392	1.397	1.390	1.398	1.391	1.404	1.397
C_4–C_5	1.380	1.403	1.397	1.401	1.395	1.402	1.396	1.407	1.401
C_5–C_6	1.358	1.396	1.392	1.394	1.389	1.396	1.391	1.401	1.396
				Angles [°]					
β	81.8	82.2	81.2	82.1	81.5	82.1	81.3	81.7	80.8
γ	6.4	0.1	1.3	0.2	1.6	0.2	1.5	0.8	1.5
τ	53.6	54.1	53.1	54.1	53.3	54.1	53.1	54.0	53.1
θ	57.8	57.8	58.0	57.8	58.0	57.8	58.0	58.1	58.4

	Gaussian							
	PBE		B3LYP		B3LYP*		PBE1PBE	
	TZVP	6-311+G**	TZVP	6-311+G**	TZVP	6-311+G**	TZVP	6-311+G**
				Bond lengths [Å]				
Fe–N	1.975	1.971	2.027	2.022	2.013	2.008	1.998	1.993
N–C_2	1.369	1.371	1.356	1.358	1.359	1.361	1.350	1.352
N–C_6	1.353	1.356	1.342	1.344	1.344	1.347	1.337	1.339
C_2–C_2'	1.464	1.466	1.473	1.475	1.471	1.473	1.468	1.470
C_2–C_3	1.400	1.402	1.394	1.396	1.395	1.397	1.389	1.391
C_3–C_4	1.392	1.394	1.387	1.389	1.388	1.390	1.384	1.386
C_4–C_5	1.397	1.399	1.389	1.391	1.390	1.393	1.386	1.388
C_5–C_6	1.391	1.394	1.386	1.389	1.387	1.390	1.383	1.386
				Angles [°]				
β	81.5	81.6	80.3	80.5	80.6	80.8	80.9	81.0
γ	3.3	3.0	3.4	3.1	3.4	3.0	3.3	2.8
τ	54.2	54.4	53.1	53.3	53.4	53.6	53.7	53.9
θ	58.3	58.3	58.7	58.7	58.6	58.6	58.6	58.5

the PBE1PBE functionals [Eqs. (10) and (11)], using the TZVP basis set.

The effect is somewhat less pronounced for the PBE1PBE functional. This behaviour is reminiscent of the tendency of the HF method to systematically predict metal–ligand bonds which are too long.[39] Thus, for $[Fe(bpy)_3]^{2+}$ in the LS state, HF calculations give values of the Fe–N bond length of 2.140 Å (TZVP) and 2.136 Å (6-311+G**), which correspond to an overestimation of the experimental bond length by as much as ≈0.2 Å.

Table 2. Optimised $[Fe(bpy)_3]^{2+}$ geometries in the HS ^5E state: ADF results.

	BP86		PW91		PBE		RPBE	
	DZ	TZP	DZ	TZP	DZ	TZP	DZ	TZP
				Bond lengths [Å]				
Fe–N	2.158	2.182	2.148	2.174	2.158	2.178	2.192	2.220
N–C_2	1.375	1.361	1.373	1.359	1.374	1.360	1.380	1.366
N–C_6	1.363	1.349	1.360	1.347	1.362	1.348	1.368	1.354
C_2–C_2'	1.477	1.479	1.476	1.478	1.476	1.479	1.486	1.489
C_2–C_3	1.405	1.401	1.403	1.399	1.404	1.401	1.411	1.408
C_3–C_4	1.400	1.393	1.398	1.391	1.399	1.393	1.404	1.398
C_4–C_5	1.403	1.397	1.401	1.394	1.402	1.396	1.407	1.401
C_5–C_6	1.397	1.392	1.395	1.389	1.396	1.391	1.401	1.397
				Angles [°]				
β	76.5	75.4	76.7	75.6	76.4	75.5	75.7	74.6
γ	4.5	4.6	4.0	5.1	4.4	5.0	4.3	5.8
τ	46.6	46.0	47.4	46.5	46.6	46.1	46.2	46.1
θ	58.8	59.3	58.9	59.3	58.9	59.2	59.1	59.9

4.2.2. Geometries in the HS States

Tables 2 and 3 show selected distances and the values of the angles β, γ, τ and θ which characterise the geometry of the complex in the ^5E and $^5A_1$ state, respectively. For either HS state, the values of the selected structural parameters for the series of calculations predict a similar arrangement of the ligands around the Fe centre. Despite the lack of experimental data, the consistency of the computational results inspires confidence in the quality of the predicted HS geometries. Closer inspection of the Tables shows that, as observed for the LS geometries, there is a lengthening of the Fe–N bond along with

Table 3. Optimised $[Fe(bpy)_3]^{2+}$ geometries in the HS $^5A_1$ state.

	ADF							
	BP86		PW91		PBE		RPBE	
	DZ	TZP	DZ	TZP	DZ	TZP	DZ	TZP
	Bond lengths [Å]							
Fe–N	2.180	2.204	2.169	2.198	2.171	2.201	2.207	2.244
N–C_2	1.373	1.359	1.370	1.357	1.371	1.358	1.378	1.364
N–C_6	1.360	1.347	1.358	1.345	1.359	1.346	1.365	1.352
C_2–C_2'	1.483	1.483	1.482	1.481	1.483	1.483	1.492	1.492
C_2–C_3	1.404	1.400	1.402	1.398	1.403	1.400	1.409	1.407
C_3–C_4	1.402	1.394	1.400	1.392	1.402	1.394	1.407	1.399
C_4–C_5	1.402	1.395	1.400	1.393	1.401	1.395	1.406	1.400
C_5–C_6	1.399	1.393	1.396	1.391	1.398	1.392	1.403	1.398
	Angles [°]							
β	75.5	74.4	75.8	74.6	75.7	74.5	74.9	73.6
γ	5.8	5.9	5.9	6.2	6.2	6.2	6.2	6.8
τ	45.6	44.6	46.3	46.5	46.3	44.7	46.1	44.9
θ	59.1	59.4	59.1	59.5	59.2	59.4	59.7	60.1

	Gaussian							
	PBE		B3LYP		B3LYP*		PBE1PBE	
	TZVP	6-311+G**	TZVP	6-311+G**	TZVP	6-311+G**	TZVP	6-311+G**
	Bond lengths [Å]							
Fe–N	2.206	2.203	2.234	2.232	2.228	2.225	2.211	2.207
N–C_2	1.359	1.361	1.350	1.352	1.352	1.354	1.344	1.346
N–C_6	1.347	1.349	1.339	1.341	1.341	1.343	1.334	1.336
C_2–C_2'	1.484	1.487	1.486	1.488	1.486	1.488	1.481	1.483
C_2–C_3	1.401	1.403	1.394	1.397	1.396	1.398	1.390	1.392
C_3–C_4	1.395	1.397	1.388	1.391	1.389	1.392	1.385	1.388
C_4–C_5	1.395	1.398	1.388	1.391	1.390	1.392	1.385	1.388
C_5–C_6	1.394	1.396	1.387	1.389	1.388	1.391	1.384	1.386
	Angles [°]							
β	74.5	74.6	73.7	73.7	73.9	74.0	74.0	74.1
γ	8.9	7.5	7.1	6.1	7.2	6.2	7.2	5.8
τ	46.1	46.1	45.3	45.2	45.4	45.4	45.6	45.6
θ	59.9	59.9	60.1	60.1	60.1	60.0	60.0	60.0

a shrinking of the aromatic rings with increasing quality of the basis set. As also observed for the LS geometries, for the $^5A_1$ geometries the use of the hybrids leads to the least-expanded pyridinyl rings and the longest Fe–N bonds are obtained for the RPBE and hybrid functionals. Again for the hybrids the Fe–N bond lengthens with the amount a_0 of the exact-exchange contribution (see Figure 8). One notes 1) that the dependence is more pronounced for the B3LYP functional than for the PBE1PBE functional; and 2) that, for both functionals, the Fe–N bond length varies with a_0 slightly less rapidly for the complex in the HS state than for the complex in the LS state, as shown by the plots of Δr_{HL} against a_0 in the inset of Figure 8. At the HF level, an Fe–N bond length of 2.284 Å is obtained for the complex in the HS $^5A_1$ state. It is longer than those obtained with the XC density functionals with differences of as much as $\approx$0.1 Å (Table 3). However the discrepancy between the HF and DFT metal–ligand distances turns out to be less marked in the HS state than in the LS state, thus showing that the consequences of the neglect of the correlation in the ab initio calculations are less dramatic in the HS state than in the LS state. For the DFT results, it appears that, as a whole, the influence of the basis sets and of the functionals on the calculated geometries is the same whenever one considers either the LS geometries or the HS geometries. It follows that any bias due to the methods used will have a limited impact on the results of the comparison between the predicted geometries of the complex in the different states.

Thus, irrespective of the theoretical level considered, the main structural difference when going from the ^5E state to the $^5A_1$ state turns out to be the lengthening of $\approx$0.02 Å of the Fe–N bond which barely affects the bond lengths within the ligands (Tables 2 and 3). The $^5E \rightarrow {}^5A_1$ change of state foremost consists in the depopulation of the 44e spin-down level in favour of the $25a_1$ spin-down level (Figures 5 and 6). These levels of $Fe(t_{2g})$ parentage being nonbonding is the reason as to why the geometries of the ligands hardly vary. The lengthening of the Fe–N bond may be explained by the fact 1) that there is a transfer of electron density from the *xy*-plane to along the *z* axis and 2) that the increase of the density along *z* tends to repel the ligands.

4.3. Structural Changes with Regard to the Analysis of the Low-Temperature Relaxation Dynamics

Comparison of Tables 1–3 shows that the most important structural change upon the LS→HS transition is found for the Fe–N bond which lengthens by about 0.2 Å. Table 4 gives for all the considered theoretical levels the estimated Δr_{HL} values.

Table 4. Comparison between calculated Fe–N bond-length differences $\Delta r_{HL} = r_{HS} - r_{LS}$ (Å), (where r_{HS} and r_{LS} are the Fe–N bond lengths in the HS (^5E or $^5A_1$) and LS ($^1A_1$) states, respectively), and experimental Δr_{HL} values for spin-crossover systems with $[FeN_6]$ coordination.[5–11]

	Δr_{HL}			Δr_{HL}
	^5E	$^5A_1$		$^5A_1$
BP86/DZ	0.202	0.224	PBE/TZVP	0.231
BP86/TZP	0.204	0.224	PBE/6-311+G**	0.232
PW91/DZ	0.194	0.215	B3LYP/TZVP	0.207
PW91/TZP	0.203	0.227	B3LYP/6-311+G**	0.210
PBE/DZ	0.203	0.216	B3LYP*/TZVP	0.215
PBE/TZP	0.203	0.226	B3LYP*/6-311+G**	0.217
RPBE/DZ	0.213	0.228	PBE1PBE/TZVP	0.213
RPBE/TZP	0.217	0.241	PBE1PBE/6-311+G**	0.214
Exp.: $\Delta r_{HL} \approx 0.16$–$0.22$				

Table 5. Comparison between calculated differences in molecular volume, $\Delta V_{HL} = V_{HS} - V_{LS}$ (in Å^3), (where V_{HS} and V_{LS} are the molecular volumes in the HS (^5E or $^5A_1$) and LS ($^1A_1$) states, respectively), and measured changes of crystal volume per molecular unit, ΔV_{HL}^{exp}.[8, 12–14]

	V_{LS}	V_{HS}		ΔV_{HL}	
		^5E	$^5A_1$	^5E	$^5A_1$
BP86/DZ	720	748	749	28	29
BP86/TZP	670	691	693	21	23
PW91/DZ	717	743	744	26	27
PW91/TZP	666	688	689	22	23
PBE/DZ	718	747	745	29	27
PBE/TZP	668	689	690	21	22
RPBE/DZ	725	755	753	30	28
RPBE/TZP	671	693	695	22	24
Exp: $\Delta V_{HL} \approx 15$–30					

This increase of the Fe–N distance is due to the promotion of two electrons from the nonbonding metallic levels of octahedral Fe(t_{2g}) parentage into the antibonding level of octahedral Fe(e_g) parentage. It entails an important spatial rearrangement of the ligands illustrated by the relatively large variations of the angles β, γ, τ, and θ. Within the ligands, the C_2–C_2' distance between the pyridinyl moieties gets longer by about 0.02 Å, probably because it permits—along with the modification of the angle values—the optimal metal–ligand interactions despite the lengthening of the Fe–N bond. The other C–C bonds and the C–H bonds are hardly affected. The N–C distances become shorter by ≈ 0.01 Å; however the N–C_2 bond remains longer than the N–C_6 bond as in the experimental LS geometry. The shortening of both N–C bonds with increasing metal–ligand distance can be assigned to a decrease of π-backbonding involving ligand-centred orbitals with antibonding character at the level of the N–C bonds. Nevertheless, the changes in bond lengths observed for the ligands are globally quite limited and this actually is in agreement with the known rigidity of the 2,2′-bipyridine ligand. The difference of ≈ 0.2 Å for the metal–ligand bond between the LS and the HS states agrees remarkably well with the experimental values found for iron(II) spin-crossover compounds with the same $[FeN_6]$ first coordination sphere as $[Fe(bpy)_3]^{2+}$ and, in particular, it validates the assumption $\Delta r_{HL} \approx 0.2$ Å central to the analysis of the relaxation dynamics.

The molecular volume variation, ΔV_{HL}, also plays an important role because it governs the influence of an exerted pressure on the relaxation dynamics. In order to probe this value, the molecular volume of the complex in the LS and HS states was calculated as the volume defined by the isodensity surface 0.0004 e bohr^{-3}. This charge density value was used as it is known to yield volumes for organic compounds that compare well with the observed molar volumes in the liquid phase.[85,86] Calculations were done for the complex in the $^1A_1$, ^5E and $^5A_1$ states using the STO DZ and TZP basis sets and the BP86, PW91, PBE and RPBE functionals. The results are reported in Table 5.

One notes that the LS and HS molecular volumes obtained using the DZ basis set are systematically larger than the corresponding ones obtained with the TZP basis sets by ≈ 50 and ≈ 40 Å^3, respectively. This can be explained by the previously noticed fact that the geometries found for the ligands using the DZ basis set are more expanded than those found using the TZP basis set. Nevertheless, the ΔV_{HL} values calculated using either basis set are comparable. Depending on the functional used it is between 26 and 30 Å^3 for the DZ basis set and between 21 and 24 Å^3 for the TZP basis sets. These values are in the 15–30 Å^3 range observed experimentally for spin-crossover systems and they agree remarkably well with the model value of 25 Å^3 estimated from the pressure dependence of the HS→LS relaxation in $[Fe(bpy)_3]^{2+}$ under the assumption that $\Delta r_{HL} \approx 0.2$ Å.

4.4. The HS–LS Energy Gap

The zero-point energy difference ΔE_{HL}^{o} of $[Fe(bpy)_3]^{2+}$ doped into different crystalline hosts has been estimated in Section 2 from the low-temperature HS→LS relaxation dynamics to lie in the range of 2500–5000 cm^{-1} based on the now-validated assumption that $\Delta r_{HL} \approx 0.2$ Å. The purely electronic energy difference between the potential wells of the lowest component of the HS state and the LS state is given by $\Delta E_{HL}^{el.} = \Delta E_{HL}^{o} - \Delta E_{HL}^{vib.}$. The vibrational contribution, $\Delta E_{HL}^{vib.}$, was estimated to be -875 cm^{-1} from a vibrational analysis performed at the TZVP/PBE level for the LS $^1A_1$ and the HS $^5A_1$ states. The sign reflects the weakening of the metal–ligand bond when passing from the LS to the HS state.[87] Thus the best experimental estimate of $\Delta E_{HL}^{el.}$ for $[Fe(bpy)_3]^{2+}$ is in the range of 3500–6000 cm^{-1}. The comparison of the calculated values of $\Delta E_{HL}^{el.}$ with this estimate will provide a stringent test of the performance of the functionals used in this study.

Table 6 summarises the calculated values of the electronic energy difference between the HS and the LS state, $\Delta E_{HL}^{el.}$, of $[Fe(bpy)_3]^{2+}$ for the STO DZ and TZP basis sets (ADF) and for the GTO 6-311+G** and TZVP basis sets (Gaussian), and Figure 9 shows a graphic representation of the calculated values of $\Delta E_{HL}^{el.}$ versus the respective calculated Fe–N bond lengths. Results obtained using Gaussian are restricted to the $^5A_1$ component of the HS state. ADF permits calculations on both components of the HS state, which show that the energy difference between the $^5A_1$ and the ^5E components is compara-

Table 6. Calculated and experimental (see text) electronic energy differences $\Delta E^{el.}_{HL}$ (in cm^{-1}).

	$\Delta E^{el.}_{HL}$			$\Delta E^{el.}_{HL}$
	^5E	$^5A_1$		$^5A_1$
BP86/DZ	14397	15169	PBE/TZVP	11373
BP86/TZP	11034	11135	PBE/6-311+G**	11849
PW91/DZ	15055	15879	B3LYP/TZVP	766
PW91/TZP	11699	11887	B3LYP/6-311+G**	1211
PBE/DZ	14431	15313	B3LYP*/TZVP	3432
PBE/TZP	11022	11337	B3LYP*/6-311+G**	3907
RPBE/DZ	10463	10853	PBE1PBE/TZVP	−951
RPBE/TZP	6909	6640	PBE1PBE/6-311+G**	−466
Exp.: $\Delta E^{el.}_{HL} \approx 3500–6000$				

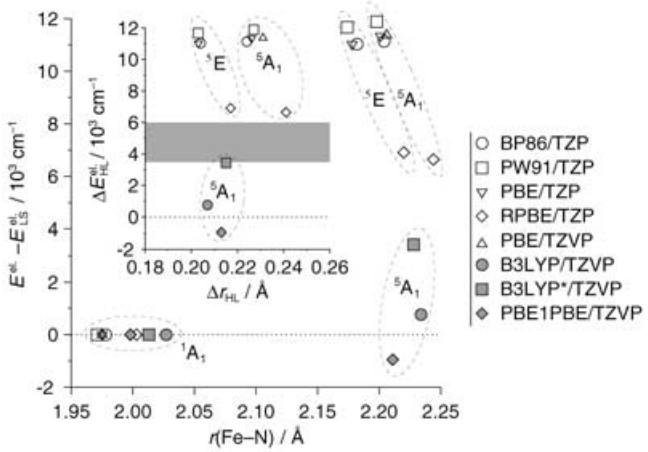

Figure 9. Comparison of the best DFT estimates of the relative positions of the LS $^1A_1$ and HS ^5E and $^5A_1$ states of $[Fe(bpy)_3]^{2+}$ along the Fe–N distance coordinate: results are for ADF and Gaussian calculations with the STO TZP and GTO TZVP basis sets. The electronic energy is given relative to the energy of the LS state. Inset: HS--LS electronic energy difference $\Delta E^{el.}_{HL}$ as a function of the Fe–N bond-length change; the shaded region indicates the 3500–6000 cm^{-1} experimental range.

tively small, irrespective of the quality of the basis set and the functional used. The calculated values for $\Delta E^{el.}_{HL}$ range from -1000 to 16000 cm^{-1}. Even though the experimental estimate lies within this range, this large spread is clearly not satisfactory and needs further discussion. Nevertheless, it must be mentioned that these DFT results are far better than the HF results since, for a computational effort comparable to the one of the calculations with the hybrids, the uncorrelated ab initio calculations give severely underestimated $\Delta E^{el.}_{HL}$ values of -25126 (TZVP) and -24364 cm^{-1} (6-311+G**).

In principle, the performance of different density functionals can only be judged in the limit of a complete basis set. In practice, one is often obliged to test functionals using incomplete basis sets. Before discussing the functionals, let us focus on the influence of the basis set on the evaluation of $\Delta E^{el.}_{HL}$. For a given functional the DZ basis set results in values of $\Delta E^{el.}_{HL}$ for the ^5E and the $^5A_1$ components which are systematically higher by $\approx$3400 and $\approx$4000 cm^{-1}, respectively, compared to the values obtained with the TZP basis set. The improvement of the quality of the basis set actually lowers the energy of $[Fe(bpy)_3]^{2+}$ in either spin-state, however, the effect is more pronounced for the complex in the HS state than in the LS state. This is due to the limitations tied to the use of the smaller DZ basis set becoming more important as the metal–ligand bond lengthens. Thus the decrease in $\Delta E^{el.}_{HL}$ of $\approx$3400 cm^{-1} for the ^5E component is associated with the lengthening of the metal–ligand bond by 0.19–0.22 Å. Similarly, the Fe–N bond in the $^5A_1$ state being $\approx$0.02 Å longer than in the ^5E state, the change of basis set lowers the HS–LS energy gap by another $\approx$600 cm^{-1}. These variations illustrate the effect of cancellation of errors tied to the use of finite basis sets. That is, the cancellation of errors is more effective 1) the smaller the difference in metal–ligand bond lengths in given geometries, and 2) the more flexible the basis set is for the description of the valence electrons hence of chemical bonding. In addition, the $^5A_1$–$^1A_1$ electronic energy difference evaluated with the PBE functional and using the STO TZP and the GTO TZVP basis sets in ADF and Gaussian, respectively, differ by only 36 cm^{-1}. This firmly establishes the previously noted equivalence of the STO TZP and the GTO TZVP basis sets and the order of increasing quality as shown in Equation (12):

$$DZ \ll TZP \equiv TZVP \quad (12)$$

For the two GTO basis sets, $\Delta E^{el.}_{HL}$ is typically $\approx$440 cm^{-1} larger for the 6-311+G** basis set than for the TZVP basis set, irrespective of the functional. As the 6-311+G** basis set offers a larger flexibility for the description of the valence electrons than the TZVP basis set, this suggests that the use of basis sets larger than those we have used would mainly result in a slight stabilisation of the LS state with respect to the HS state, that is, in a slight increase of $\Delta E^{el.}_{HL}$ as observed when passing from the TZVP to the 6-311+G** basis set. Finally, the comparison of the sizes of the basis sets and of the results they lead to indicates that, among the basis sets used, the TZVP and the TZP basis set offer the best trade-off between size and flexibility.

The above discussion shows that the quality of the basis set influences the calculations quite considerably and therefore in the following the discussion of the performance of the functionals is restricted to results obtained using the two high-quality TZVP and TZP basis sets and to the comparison of $\Delta E^{el.}_{HL}$ for the $^5A_1$ component as only this one is accessible with Gaussian. We note that the GGA functionals BP86, PW91 and PBE give values for $\Delta E^{el.}_{HL}$ of 11000–12000 cm^{-1}, thus systematically overestimating it by more than 5000 cm^{-1} compared to the experimental value. On the other hand the hybrid functionals B3LYP and PBE1PBE underestimate $\Delta E^{el.}_{HL}$ by at least 3000 cm^{-1}, in fact falsely predicting $[Fe(bpy)_3]^{2+}$ to be a spin-crossover or even a high-spin complex. Two of the functionals, namely the RPBE GGA and the B3LYP* hybrid, with calculated values of $\Delta E^{el.}_{HL}$ of 6640 and 3430 cm^{-1}, respectively, approach the range of the experimental estimate. In contrast to the optimised geometries, the nature of the functional used has an even greater influence on the calculated values of $\Delta E^{el.}_{HL}$ than the basis set, and therefore the energetics provide a much more stringent test of the performance of a given functional than the geome-

try optimisation. Based on this criterion, the RPBE GGA and the B3LYP* hybrid functionals show the best performance.

The disparity in performance of the XC functionals for predicting $\Delta E^{el.}_{HL}$ of the $[Fe(bpy)_3]^{2+}$ complex points to the inherent difficulty of XC functionals to predict the relative energies of states of different spin multiplicities correctly, particularly for spin-crossover systems[27,49,60–62] but also for spin-forbidden chemical reactions.[88] This is emphasised by the fact that for the TZP basis set the ^5E and the $^5A_1$ components of the quintet state are consistently predicted to be nearly degenerate, that is within the chemical accuracy of 350 cm^{-1}, by functionals which behave quite differently when it comes to evaluating the HS--LS energy gap. Given that the PBE, RPBE and PBE1PBE functionals have the same correlation contribution but differ in the exchange contribution, the remarkable divergence between their estimates of $\Delta E^{el.}_{HL}$ must be due to the difficulty in correctly treating the exchange contribution in the approximate functionals. The key point is that the approximate exchange functionals have to account for the variation of the exchange interaction (Fermi correlation) correctly, hence of $|E_X|$, with increasing or decreasing spin polarisation as in the case of a change of spin-state. For the GGA functionals, this implies that the exchange enhancement factor F_X intervening in the definition of E_X^{GGA} [Eq. (9)] has to increase correctly with the reduced spin-density gradients $s_\alpha(\mathbf{r})$ so as to depart rapidly from its LDA value of $F_X(0)=1$ and thus to overcome the underestimation of the exchange energy inherited from their LDA component for both spin-unpolarised and spin-polarised systems. For spin-unpolarised systems with $\rho_\uparrow(\mathbf{r})=\rho_\downarrow(\mathbf{r})=\rho(\mathbf{r})/2$, Figure 10 allows the comparison of the enhancement factors of the B88, PW91, PBE and RPBE exchange functionals.

Therein F_X is plotted against the reduced charge-density gradient, $s(\mathbf{r})=|\nabla\rho(\mathbf{r})|/[2(3\pi^2)^{1/3}\rho^{4/3}(\mathbf{r})]$, for $s\in[0,3]$, that is, for s in the range which is energetically important for atomic and molecular systems.[43] For the purpose of our discussion, it suffices to note that 1) the four F_X functions increase with s and are almost superimposable for $0\le s\le 0.7$, 2) in the most significant interval $0.7\le s\le 2$, the F_X^{PW91}, F_X^{PBE} and even the F_X^{B88} enhancement factors still behave quite similarly, but F_X^{RPBE} is found to be larger than the three other functions everywhere in this range. Of the four GGA exchange functionals, the RPBE thus provides the largest nonlocal corrections to the LDA exchange energy for the spin-unpolarised case.

For spin-polarised systems, the gradient correction is even more important since the exchange interactions increase with the spin polarisation $\zeta(\mathbf{r})=[\rho_\uparrow(\mathbf{r})-\rho_\downarrow(\mathbf{r})]/\rho(\mathbf{r})$. The dependence of E_X^{GGA} on $\rho(\mathbf{r})$ is made more obvious by recasting Equation (9) in the form of Equation (13):

$$E_X^{GGA}[\rho_\uparrow,\rho_\downarrow]=C_X\int d\mathbf{r}\rho^{4/3}(\mathbf{r})F_X[\zeta(\mathbf{r}),s(\mathbf{r})] \qquad (13)$$

The exchange enhancement factor $F_X(\zeta,s)$, derived by setting $\rho_\uparrow=\rho(1+\zeta)/2$ and $\rho_\downarrow=\rho(1-\zeta)/2$ in Equation (9) and by neglecting contributions in $\nabla\zeta$,[43] gives Equation (14):

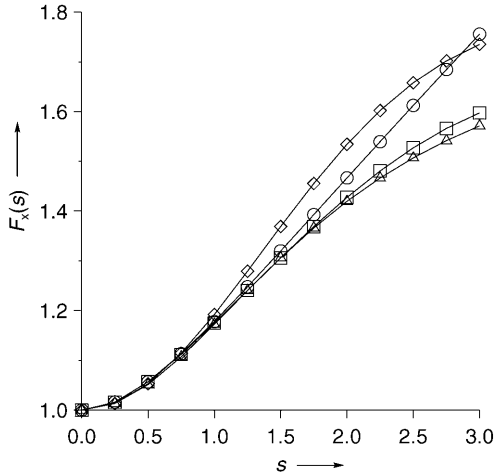

Figure 10. Plot of the exchange enhancement factors F_X for the B88 (●), PW91 (■), PBE (▲) and RPBE (◆) exchange functionals against the reduced charge-density gradient $s(\mathbf{r})=|\nabla\rho(\mathbf{r})|/[2(3\pi^2)^{1/3}\rho^{4/3}(\mathbf{r})]$ (results for the spin-unpolarised case).

$$F_X(\zeta,s)=\frac{1}{2}(1+\zeta)^{4/3}F_X[s/(1+\zeta)^{1/3}]+\frac{1}{2}(1-\zeta)^{4/3}F_X[s/(1-\zeta)^{1/3}] \qquad (14)$$

$F_X(\zeta,s)$ is represented in Figure 11, along with the gradient correction $F_X(\zeta,s)-F_X(\zeta,s=0)$, for the B88, PW91, PBE and RPBE exchange functionals as function of ζ for $s=0.0$, 0.5, 1.0, 1.5, 2. In all cases, the enhancement factor increases with the spin polarisation. For $s=0$, that is in LDA, it reduces to $F_X(\zeta,s=0)=\frac{1}{2}[(1+\zeta)^{4/3}+(1-\zeta)^{4/3}]$. The gradient corrections increase with increasing values of s. For small values of s they are quite similar for the four functionals considered. At higher values of s, that is for $s\approx 1.5$, the F_X^{RPBE} is again found to give the largest gradient correction. Therefore the success of the RPBE XC functional in correctly predicting the HS--LS energy difference in $[Fe(bpy)_3]^{2+}$ can be ascribed to an improved gradient correction to the LDA exchange energy for both spin-unpolarised and spin-polarised systems as compared to PBE, PW91 and BP86 GGAs, thus allowing a more reliable description of the change in exchange energy which accompanies the spin-state change. The requirement of correctly rendering the variation of the exchange energy upon the change of spin-state is also important because of the large metal–ligand bond-length difference between the two states as the reduced gradient s increases when bonds stretch and exchange turns on with increasing s values.[41,43]

As a cautious note, we believe at this point that it is worth insisting that the success met with the RPBE functional for the evaluation of the HS--LS energy difference in $[Fe(bpy)_3]^{2+}$, or even in $[Fe(H_2O)_6]^{2+}$ as in ref. [27], does not imply that this GGA is *the* functional of choice for the description of iron(II) complexes. For instance, for the $[Fe(NH_3)_6]^{2+}$ complex investigated in ref. [28], although the RPBE functional outperforms the BP86, BLYP, PW91 and PBE GGAs and performs as well as more recent functionals, it still underestimates the best ab initio estimate of the HS--LS energy difference, the best overall

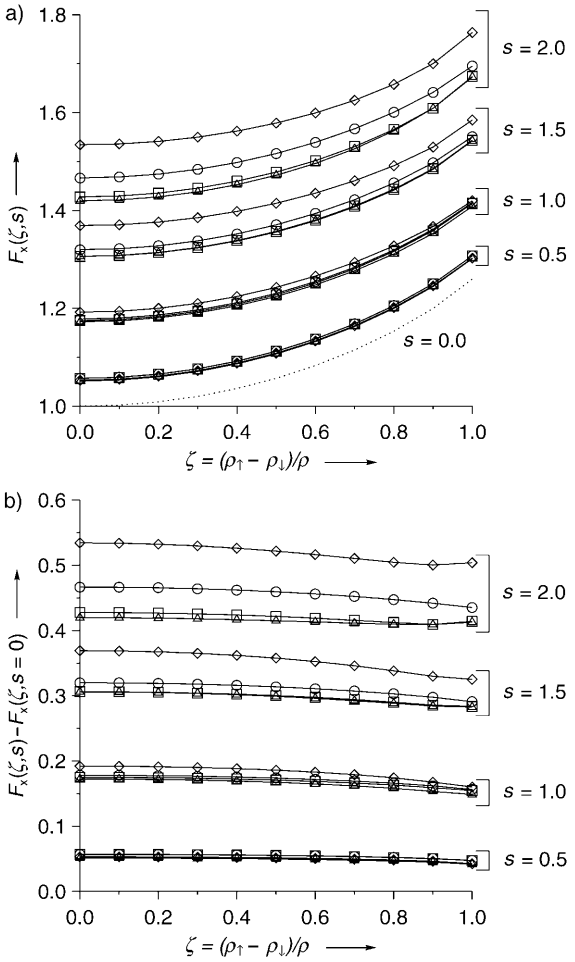

Figure 11. a) Exchange enhancement factor $F_X(\zeta,s)$ [Eq. (14)] for the B88 (●), PW91 (■), PBE (▲) and RPBE (◆) exchange functionals as a function of ζ for fixed s values. b) Plots of the gradient corrections $F_X(\zeta,s)-F_X(\zeta,s=0)$.

agreement for the energetics of the studied simple $[Fe(H_2O)_6]^{2+}$ and $[Fe(NH_3)_6]^{2+}$ complexes being found for the PBE1PBE functional.

For the hybrid functionals B3LYP [Eq. (10)] and PBE1PBE [Eq. (11)], the contribution a_0 of the exact-exchange energy E_X^{KS}, Equation (7), has a substantial influence on the evaluation of the HS--LS energy gap. Figure 12 gives $\Delta E_{HL}^{el.}$ plotted against a_0 for $0 \le a_0 \le 0.3$. In this interval $\Delta E_{HL}^{el.}$ for the two functionals are decreasing functions of a_0. They cross the 3500–6000 cm^{-1} range of the experimental $\Delta E_{HL}^{el.}$ values for a_0 values of between 0.10 and 0.15, the value $a_0 = 0.15$ being actually used in the B3LYP* functional by Reiher et al.[60,61] For an exact-exchange contribution smaller than 10%, the HS--LS energy gap is overestimated as a consequence of the underestimation of the exchange energy. This is best illustrated by considering the $a_0 = 0$ limit. Using the PBE1PBE formula, the exchange contribution reduces to the PBE exchange functional, which was shown above not to provide sufficient gradient corrections to the LDA exchange energy. With the B3LYP expression, the exchange contribution becomes $E_X^{LDA} + a_X \Delta E_X^B$ with $a_X = 0.72$. It also underestimates exchange since its GGA part consists of a drastic reduction to 72% of the Becke's 1988 nonlocal correction ΔE_X^B

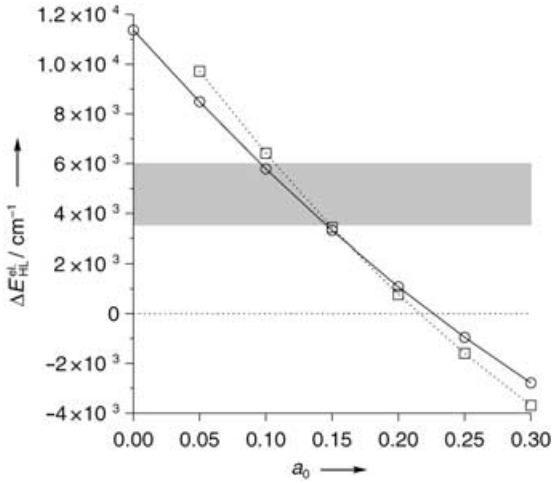

Figure 12. Dependence of the electronic energy difference $\Delta E_{HL}^{el.}$ between the HS $^5A_1$ and LS $^1A_1$ states on the a_0 coefficient of the exact-exchange contribution in the B3LYP [■ Eq. (10)] and PBE1PBE [● Eq. (11)] hybrids (results of geometry optimisations performed with the TZVP basis set). The shaded region indicates the range of the experimental values.

which was already found to be too small. With regard to the issue of the amount of the exact exchange to be included in hybrids, the above results support the idea that, for the energetics of transition metal complexes, it must be further reduced relative to its generally admitted value of about 1/4. A contribution of ≈10% seems to be the more appropriate.

We end our discussion by reconsidering the remarks made in Section 5.2 that the use of the RPBE GGA and of the hybrids yields the longest metal–ligand bonds for the complex in a given spin-state, and that the Fe–N bond obtained with a hybrid is longer the larger the contribution of the exact exchange. From the analysis of the results obtained for the energetics and the trend of the HF method to give too long metal–ligand bonds due to the lack of correlation, it actually appears that both phenomena can be explained by the fact that correlation turns off relative to exchange with an increase of the latter,[43] since 1) as compared to the other GGAs there is a relative enhancement of exchange with the RPBE provided by significant gradient corrections to the LDA exchange energy and, similarly, 2) the admixture of exact-exchange energy in hybrids is at the origin of an increase of exchange.

5. Concluding Remarks

We have examined the extension of the HS→LS relaxation model used for spin-crossover systems to the LS complex $[Fe(bpy)_3]^{2+}$. For this purpose, $[Fe(bpy)_3]^{2+}$ has been characterised in the LS and HS states using density functional approaches. The BP86, PW91, PBE and RPBE GGAs and the B3LYP, B3LYP* and PBE1PBE hybrids have been employed in combination with the STO DZ and TZP and the GTO TZVP and 6-311+G** basis sets. The main results and conclusions obtained are summarised below.

1) By applying the relaxation model to $[Fe(bpy)_3]^{2+}$, a zero-point energy difference ΔE^{o}_{HL} of between 2500 and 5000 cm^{-1} was estimated for the complex embedded in different crystalline hosts and a molecular volume change of $\Delta V_{HL} \approx 25$ Å^3 was deduced from the pressure study of its relaxation dynamics. The assumption central to this approach of an Fe–N bond-length change of $\Delta r_{HL} \approx 0.2$ Å was validated at all the considered theoretical levels, and the calculations furthermore gave ΔV_{HL} values in good agreement with the experimental estimate. These results therefore establish the validity of the extension of the relaxation model used for the spin-crossover complexes to the LS complex $[Fe(bpy)_3]^{2+}$.
2) The density functional calculations led to the characterisation of the D_3 complex in the $^1A_1$, ^5E and $^5A_1$ states which were shown to correspond to the octahedral ligand-field LS $^1A_{1g}(t_{2g}^6)$ and HS $^5T_{2g}(t_{2g}^4e_g^2)$ states, the quintet states resulting from the trigonal splitting of the octahedral HS state. The spin-state change from the LS state to any of the HS component schematically corresponds to the promotion of two electrons from the frontier nonbonding a_1 and e KS levels of octahedral Fe(t_{2g}) parentage into the frontier antibonding KS e level of octahedral Fe(e_g) parentage. This explains the large increase of the Fe–N bond distance of about 0.2 Å upon the change of spin states which constitutes the main structural evolution in the complex. With regard to the HS geometries, they are quite similar as the difference in their electronic structure essentially involves an electronic rearrangement within the frontier nonbonding KS levels of octahedral Fe(t_{2g}) parentage.
3) The STO TZP and GTO TZVP basis sets proved to be of similar quality for the description of the geometry and the energetics of $[Fe(bpy)_3]^{2+}$. They outperform the small STO DZ basis set and constitute thus the best basis sets used.
4) Whereas the XC functionals consistently describe the LS and HS geometries, they perform very differently with respect to the energetics. For the calculations with the most flexible and equivalent TZP and TZVP basis sets, the HS--LS electronic energy difference that comes closest to the best experimental estimate of 3500–6000 cm^{-1} is obtained with the RPBE GGA ($\Delta E^{el.}_{HL} = 6640$ cm^{-1}). This energy gap is overestimated when the BP86, PW91 and PBE GGAs are used (11000–12000 cm^{-1}) and it is underestimated with the hybrids. With the B3LYP ($\Delta E^{el.}_{HL} = 766$ cm^{-1}) and PBE1PBE (-951 cm^{-1}) hybrids, $[Fe(bpy)_3]^{2+}$ is wrongly predicted as a spin-crossover or HS complex. The result improves with the B3LYP* hybrid ($\Delta E^{el.}_{HL} = 3432$ cm^{-1}), which incorporates less exact-exchange contribution than the B3LYP. We ascribe the difficulties met with the DFT methods for the evaluation of the HS--LS energy gap in $[Fe(bpy)_3]^{2+}$ to the fact that the exchange functionals do not properly take into account the variation of exchange when the spin polarisation and the metal–ligand bond length significantly vary, as is the case upon the change of spin-state in our system. This deficiency is emphasised by the fact that the HS ^5E and $^5A_1$ states of a same spin multiplicity are consistently given by all the GGAs as being nearly degenerate to within 350 cm^{-1} (4 kJ mol^{-1}). The overestimation of $\Delta E^{el.}_{HL}$ with the GGAs is due to the fact that, despite the nonlocal corrections, the B88, PW91 and PBE exchange GGAs still present the underestimation of exchange inherited from their LDA component. The larger gradient correction of the RPBE exchange GGA allows a better description of exchange which is at the origin of the very good result achieved for the determination of $\Delta E^{el.}_{HL}$ with this functional. With the hybrids, exchange is overestimated and this explains the severe underestimation of $\Delta E^{el.}_{HL}$ with the B3LYP and PBE1PBE functionals. For the hybrids, the determination of the dependence of the HS--LS energy difference on the exact-exchange contribution shows that the contribution in both the B3LYP and PBE1PBE functionals should be reduced to an amount of about 10% to achieve a good description of the energetics of $[Fe(bpy)_3]^{2+}$.

Our results show that a reliable characterisation of the $[Fe(bpy)_3]^{2+}$ complex in the LS and HS states can be achieved using density functional approaches but also that there is still room for improving the XC functionals. With regard to the correlation functionals, although their formal properties differ,[54,55,89] we cannot distinguish between them. Given that exchange dominates the high-density limit,[63,64] the evaluation of the energy difference between states of different multiplicities for electron-rich system such as iron(II) complexes suffers mainly from the limitation of the exchange functionals. The difficulties encountered for the energetics suggest that the relative spin-state energies of a number of systems should be incorporated into the data sets that serve as benchmarks for XC functionals or as training sets for their empirical design. To improve our understanding of the photophysical properties of $[Fe(bpy)_3]^{2+}$ further and, in particular with regard to the dynamics of the photo-induced HS→LS relaxation, the role of the environment must now be thoroughly investigated. In that respect, we have extended our study so as to account for the influence of solvation effects on the HS--LS energy gap and on the optical and chiroptical properties of the complex.[90]

Acknowledgements

We would like to thank Nabil Berkaïne and Georg Ganzenmüller for helpful discussions. A.H., A.V. and L.M.L.D. thank the Centro Svizzero di Calcolo Scientifico (CSCS) for the calculation resources allocated in the framework of the CSCS project entitled "Photophysics and Photochemistry of Transition Metal Compounds: Theoretical Approaches" and the Swiss National Science Foundation for financial support. This is part of a contribution by A.F. and M.E.C. to the groupe de recherche in "density functional theory" (DFT) and the COST working group D26/0013/02. A.F. thanks the French Ministère de l'Education Nationale et de la Recherche for a Bourse de Mobilité. M.E.C. and A.F. thank the support team of the LEDSS and the Centre d'Experimentation pour le Calcul Intensif en Chimie (CECIC) and they acknowledge supercomputer time at the Institut du Développement et des Ressources en Informatique Scientifique (IDRIS project number 021576).

Keywords: density functional calculations · iron(II) complexes · time-resolved spectroscopy · high-spin–low-spin relaxation · spin crossover

[1] *Topics in Current Chemistry, Vol.* 233 (Eds.: P. Gütlich, H. A. Goodwin), Springer-Verlag, Heidelberg, **2004**.
[2] *Topics in Current Chemistry, Vol.* 234 (Eds.: P. Gütlich, H. A. Goodwin), Springer-Verlag, Heidelberg, **2004**.
[3] *Topics in Current Chemistry, Vol.* 235 (Eds.: P. Gütlich, H. A. Goodwin), Springer-Verlag, Heidelberg, **2004**.
[4] P. Gütlich, H. A. Goodwin in *Topics in Current Chemistry, Vol.* 233 (Eds.: P. Gütlich, H. A. Goodwin), Springer-Verlag, Heidelberg, **2004,** 1 – 47.
[5] M. A. Hoselton, L. J. Wilson, R. S. Drago, *J. Am. Chem. Soc.* **1975**, *97*, 1722 – 1729.
[6] B. A. Katz, C. E. Strouse, *J. Am. Chem. Soc.* **1979**, *101*, 6214 – 6221.
[7] M. Mikami-Kido, Y. Saito, *Acta Crystallogr.* **1982**, *B38*, 452 – 455.
[8] R. A. Binstead, J. K. Beattie, *Inorg. Chem.* **1986**, *25*, 1481 – 1484.
[9] M. Konno, M. Mikami-Kido, *Bull. Chem. Soc. Jpn.* **1991**, *64*, 339 – 345.
[10] J.-F. Létard, P. Guionneau, L. Rabardel, J. A. K. Howard, A. E. Goeta, D. Chasseau, O. Kahn, *Inorg. Chem.* **1998**, *37*, 4432 – 4441.
[11] P. J. Koningsbruggen, Y. Garcia, O. Kahn, L. Fournès, H. Kooijman, A. L. Spek, J. G. Haasnoot, J. Moscovici, K. Provost, A. Michalowicz, F. Renz, P. Gütlich, *Inorg. Chem.* **2000**, *39*, 1891 – 1900.
[12] L. Wiehl, G. Kiel, C. P. Köhler, H. Spiering, P. Gütlich, *Inorg. Chem.* **1986**, *25*, 1565 – 1571.
[13] P. Adler, A. Hauser, A. Vef, H. Spiering, P. Gütlich, *Hyperfine Interact.* **1989**, *47*, 343 – 356.
[14] L. Wiehl, H. Spiering, P. Gütlich, K. Knorr, *J. Appl. Cryst.* **1990**, *23*, 151 – 160.
[15] A. Hauser, N. Amstutz, S. Delahaye, A. Sadki, S. Schenker, R. Sieber, M. Zerara, *Struct. Bonding*, **2004**, *106*, 81 – 96.
[16] J. J. McGarvey, I. Lawthers, *J. Chem. Soc., Chem. Comm.* **1982**, 906 – 907.
[17] I. Lawthers, J. J. McGarvey, *J. Am. Chem. Soc.* **1984**, *106*, 4280 – 4282.
[18] S. Decurtins, P. Gütlich, C. P. Köhler, H. Spiering, A. Hauser, *Chem. Phys. Lett.* **1984**, *105*, 1 – 4.
[19] S. Decurtins, P. Gütlich, K. M. Hasselbach, H. Spiering, A. Hauser, *Inorg. Chem.* **1985**, *24*, 2174 – 2178.
[20] E. Buhks, G. Navon, M. Bixon, J. Jortner, *J. Am. Chem. Soc.* **1980**, *102*, 2918 – 2923.
[21] C.-L. Xie, D. N. Hendrickson, *J. Am. Chem. Soc.* **1987**, *109*, 6981 – 6988.
[22] A. Hauser, *Comments Inorg. Chem.* **1995**, *17*, 17 – 40, and references therein.
[23] A. Vef, U. Manthe, P. Gütlich, *J. Chem. Phys.* **1994**, *101*, 9326 – 9332.
[24] P. Gütlich, A. Hauser, H. Spiering, *Angew. Chem.* **1994**, *106*, 2109 – 41; *Angew. Chem. Int. Ed. Engl.* **1994**, *33*, 2024 – 2054.
[25] A. Hauser, P. Gütlich, H. A. Goodwin in *Topics in Current Chemistry, Vol.* 233 (Eds.: P. Gütlich, H. A. Goodwin), Springer-Verlag, Heidelberg, **2004**, pp. 49 – 58.
[26] A. Hauser, P. Gütlich, H. A. Goodwin in *Topics in Current Chemistry, Vol.* 234 (Eds.: P. Gütlich, H. A. Goodwin), Springer-Verlag, Heidelberg, **2004**, pp. 155 – 198.
[27] A. Fouqueau, S. Mer, M. E. Casida, L. M. Lawson Daku, A. Hauser, T. Mineva, *J. Chem. Phys.* **2004**, *120*, 9473 – 9486.
[28] A. Fouqueau, M. E. Casida, L. M. Lawson Daku, A. Hauser, F. Neese, *J. Chem. Phys.* **2005**, *122*, 044110.
[29] A. Hauser, *Chem. Phys. Lett.* **1990**, *173*, 507 – 512.
[30] S. Deisenroth, A. Hauser, H. Spiering, P. Gütlich, *Hyperfine Interact.* **1994**, *93*, 1573 – 1577.
[31] S. Schenker, A. Hauser, W. Wang, I. Y. Chan, *Chem. Phys. Lett.* **1998**, *297*, 281 – 286.
[32] A. Hauser, A. Vef, P. Adler, *J. Chem. Phys.* **1991**, *95*, 8710 – 8717.
[33] S. Schenker, A. Hauser, W. Wang, I. Y. Chan, *J. Chem. Phys.* **1998**, *109*, 9870 – 9878.
[34] P. Hohenberg, W. Kohn, *Phys. Rev.* **1964**, *136*, B864 – B871.
[35] W. Kohn, L. J. Sham, *Phys. Rev.* **1965**, *140*, A1133 – A1138.
[36] O. Gunnarsson, B. I. Lundqvist, *Phys. Rev. B.* **1976**, *13*, 4274 – 4298.
[37] R. G. Parr, W. Yang, *Density Functional Theory of Atoms and Molecules*, Oxford University Press, New York, **1989**.
[38] R. M. Dreizler, E. K. U. Gross, *Density Functional Theory, An Approach to the Quantum Many-Body Problem*, Springer-Verlag, New York, **1990**.
[39] W. Koch, M. C. Holthausen, *A Chemist's Guide to Density Functional Theory*, Wiley-VCH, New York, **2000**.
[40] J. P. Perdew, M. Ernzerhof, A. Zupan, K. Burke, *J. Chem. Phys.* **1998**, *108*, 1522 – 1531.
[41] A. Zupan, K. Burke, M. Ernzerhof, J. P. Perdew, *J. Chem. Phys.* **1997**, *106*, 10184 – 10293.
[42] K. Burke, J. P. Perdew, M. Ernzerhof, *J. Chem. Phys.* **1998**, *109*, 3760 – 3771.
[43] *Lecture Notes in Physics, Vol.* 620 (Eds.: J. P. Perdew, S. Kurth. C. Fiolhais, F. Nogueira, M. Marques), Springer, Berlin, **2003**, pp. 1 – 55.
[44] A. D. Becke, *J. Chem. Phys.* **1993**, *98*, 1372 – 1377.
[45] A. D. Becke, *J. Chem. Phys.* **1993**, *98*, 5648 – 5652.
[46] J. P. Perdew, M. Ernzerhof, K. Burke, *J. Chem. Phys.* **1996**, *105*, 9982 – 9985.
[47] K. Burke, M. Ernzerhof, J. P. Perdew, *Chem. Phys. Lett.* **1997**, *265*, 115 – 120.
[48] M. Ernzerhof, *Chem. Phys. Lett.* **1996**, *263*, 499 – 506.
[49] H. Paulsen, L. Duelund, H. Winkler, H. Toftlund, A. X. Trautwein, *Inorg. Chem.* **2001**, *40*, 2201 – 2204.
[50] A. D. Becke, *Phys. Rev. A* **1988**, *38*, 3098 – 3100.
[51] C. Lee, W. Yang, R. G. Parr, *Phys. Rev. B* **1988**, *37*, 785 – 789.
[52] J. P. Perdew, J. A. Chevary, S. H. Vosko, K. A. Jackson, M. R. Pederson, D. J. Singh, C. Fiolhais, *Phys. Rev. B* **1992**, *46*, 6671 – 6687.
[53] J. P. Perdew, J. A. Chevary, S. H. Vosko, K. A. Jackson, M. R. Pederson, D. J. Singh, C. Fiolhais, *Phys. Rev. B* **1993**, *48*, 4978.
[54] J. P. Perdew, K. Burke, Y. Wang, *Phys. Rev. B* **1996**, *54*, 16533 – 16539.
[55] J. P. Perdew, K. Burke, Y. Wang, *Phys. Rev. B* **1998**, *57*, 14999.
[56] G. Baranović *Chem. Phys. Lett.* **2003**, *369*, 668 – 672.
[57] J. P. Perdew, *Phys. Rev. B* **1986**, *33*, 8822 – 8824.
[58] *Becke3LYP Method References and General Citation Guidelines*, Gaussian News, vol. 5, no. 2, summer **1994**, p. 2.
[59] S. H. Vosko, L. Wilk, M. Nusair, *Can. J. Phys.* **1980**, *58*, 1200 – 1211.
[60] M. Reiher, O. Salomon, B. A. Hess, *Theor. Chem. Acc.* **2001**, *107*, 48 – 55.
[61] O. Salomon, M. Reiher, B. A. Hess, *J. Chem. Phys.* **2002**, *117*, 4729 – 4737.
[62] M. Reiher, *Inorg. Chem.* **2002**, *41*, 6928 – 6935.
[63] J. P. Perdew, K. Burke, M. Ernzerhof, *Phys. Rev. Lett.* **1996**, *77*, 3865 – 3868.
[64] J. P. Perdew, K. Burke, M. Ernzerhof, *Phys. Rev. Lett.* **1997**, *78*, 1396.
[65] B. Hammer, L. B. Hansen, J. K. Nørskov, *Phys. Rev. B* **1999**, *59*, 7413 – 7421.
[66] F. Neese, *J. Chem. Phys.* **2003**, *119*, 9428 – 9443.
[67] C. Adamo, V. Barone, *J. Chem. Phys.* **1999**, *110*, 6158 – 6170.
[68] M. Ernzerhof, G. E. Scuseria, *J. Chem. Phys.* **1999**, *110*, 5029 – 5036.
[69] Amsterdam density functional, Theoretical Chemistry, Vrije Universiteit, Amsterdam, The Netherlands, http://www.scm.com.
[70] Gaussian 03 (Revision B.03/B.04), M. J. Frisch, G. W. Trucks, H. B. Schlegel, G. E. Scuseria, M. A. Robb, J. R. Cheeseman, J. A. Montgomery, Jr., T. Vreven, K. N. Kudin, J. C. Burant, J. M. Millam, S. S. Iyengar, J. Tomasi, V. Barone, B. Mennucci, M. Cossi, G. Scalmani, N. Rega, G. A. Petersson, H. Nakatsuji, M. Hada, M. Ehara, K. Toyota, R. Fukuda, J. Hasegawa, M. Ishida, T. Nakajima, Y. Honda, O. Kitao, H. Nakai, M. Klene, X. Li, J. E. Knox, H. P. Hratchian, J. B. Cross, C. Adamo, J. Jaramillo, R. Gomperts, R. E. Stratmann, O. Yazyev, A. J. Austin, R. Cammi, C. Pomelli, J. W. Ochterski, P. Y. Ayala, K. Morokuma, G. A. Voth, P. Salvador, J. J. Dannenberg, V. G. Zakrzewski, S. Dapprich, A. D. Daniels, M. C. Strain, O. Farkas, D. K. Malick, A. D. Rabuck, K. Raghavachari, J. B. Foresman, J. V. Ortiz, Q. Cui, A. G. Baboul, S. Clifford, J. Cioslowski, B. B. Stefanov, G. Liu, A. Liashenko, P. Piskorz, I. Komaromi, R. L. Martin, D. J. Fox, T. Keith, M. A. Al-Laham, C. Y. Peng, A. Nanayakkara, M. Challacombe, P. M. W. Gill, B. Johnson, W. Chen, M. W. Wong, C. Gonzalez, J. A. Pople, Gaussian, Inc., Pittsburgh PA, **2003**.
[71] A. Schäfer, C. Huber, R. Ahlrichs, *J. Chem. Phys.* **1994**, *100*, 5829 – 5835.
[72] K. Raghavachari, J. S. Binkley, R. Seeger, J. A. Pople, *J. Chem. Phys.* **1980**, *72*, 650 – 654.
[73] A. J. H. Wachters, *J. Chem. Phys.* **1970**, *52*, 1033 – 1036.
[74] P. J. Hay, *J. Chem. Phys.* **1977**, *66*, 4377 – 4384.
[75] K. Raghavachari, G. W. Trucks, *J. Chem. Phys.* **1989**, *91*, 1062 – 1065.
[76] K. N. Kudin, G. E. Scuseria, E. Cancès, *J. Chem. Phys.* **2002**, *116*, 8255 – 8261.

[77] MOLEKEL 4.0, P. Flükiger, H. P. Lüthi, S. Portmann, J. Weber, Swiss Center for Scientific Computing, Manno (Switzerland), **2000**.
[78] G. Schaftenaar, J. H. Noordik, *J. Comput.-Aided Mol. Design.* **2000**, *14*, 123 – 134.
[79] M. Vos, I. McCarty, *Am. J. Phys.* **1997**, *65*, 544 – 553.
[80] C. E. Brion, G. Cooper, Y. Zheng, I. V. Litvinyuk, I. E. McCarty, *Chem. Phys.* **2001**, *270*, 13 – 30.
[81] J. I. Pascual, J. Gómez-Herrero, C. Rogero, A. M. Baró, D. Sánchez-Portal, E. Artacho, P. Ordejón, J. M. Soler, *Chem. Phys. Lett.* **2000**, *321*, 78 – 82.
[82] J. Itatani, J. Levesque, D. Zeidler, H. Niikura, H. Pépin, J. C. Kieffer, P. B. Corkum, D. M. Villeneuve, *Nature* **2004**, *432*, 867 – 871.
[83] M. E. García Posse, M. A. Juri, P. J. Aymonino, O. E. Piro, H. A. Negri, E. E. Castellano, *Inorg. Chem.* **1984**, *23*, 948 – 952.
[84] S. Dick, *Z. Kristallogr.—New Cryst. Struct.* **1998**, *213*, 356.
[85] K. B. Wiberg, P. R. Rablen, D. J. Rush, T. A. Keith, *J. Am. Chem. Soc.* **1995**, *117*, 4261 – 4270.
[86] K. B. Wiberg, T. A. Keith, M. J. Frish, M. Murcko, *J. Phys. Chem.* **1995**, *99*, 9072.
[87] The negative contribution to $\Delta E_{HL}^{vib.}$ due to the frequency shifts of the vibrational modes involving the metal–ligand bond is partly counterbalanced by the increase of the frequencies of vibrational modes affecting the N–C and C–C bonds of the ligands. The increase of the frequencies of these vibrational modes centred on the aromatic rings is indicative of the diminishing of π-backbonding interactions with the lengthening of the Fe–N bond distance that imply ligand-centred antibonding orbitals.
[88] R. Poli, J. N. Harvey, *Chem. Soc. Rev.* **2003**, *32*, 1 – 8.
[89] J. P. Perdew, K. Burke, *Int. J. Quant. Chem.* **1996**, *57*, 309 – 319.
[90] A. Vargas, L. M. Lawson Daku, A. Hauser, unpublished results.

Received: December 1, 2004
Revised: March 23, 2005
Published online on June 21, 2005

